Cobalt-based magnetic nanocomposites: fabrication, fundamentals and applications

2011 J. Phys. D: Appl. Phys. 44 393001

(http://iopscience.iop.org/0022-3727/44/39/393001)

IOP PUBLISHING JOURNAL OF PHYSICS D: APPLIED PHYSICS

J. Phys. D: Appl. Phys. **44** (2011) 393001 (24pp) doi:10.1088/0022-3727/44/39/393001

TOPICAL REVIEW

Cobalt-based magnetic nanocomposites: fabrication, fundamentals and applications

Tianlong Wen[1] **and Kannan M Krishnan**

Department of Materials Science and Engineering, University of Washington, Box 352120, Seattle, WA 98195-2120, USA

E-mail: kannanmk@uw.edu

Received 6 April 2011, in final form 26 July 2011
Published 9 September 2011
Online at stacks.iop.org/JPhysD/44/393001

Abstract

Recently, magnetic nanocomposites (MNC) have aroused significant scientific and technological interests because their properties strongly rely on the interplay between those of the constituent components. Here, using three types of cobalt-based MNCs, we demonstrate how their physical behaviour, including thermal, electrical and magnetic, can be strongly affected by such interplays. First, using Au_{core}–Co_{shell} nanoparticles (NPs), we demonstrate that their thermal stabilities are critically dependent on various boundaries and they structurally transform from the core–shells to the peanut structures via several intermediate states by a series of energy minimizations including the grain boundaries, Co/Au interface and strain. Second, the microstructures of the MNC are co-determined by the properties of the individual components, which in turn will strongly affect their overall properties. We illustrate this by a careful study of the electron transport in cobalt/poly (3-hexylthiophene, 2, 5-diyl) (P3HT) hybrid thin films, and show that they satisfy a fluctuation-induced tunnelling model that is strongly depended on their microstructures; moreover, a magnetoresistance in these thin films was also observed. Finally, the magnetic properties and phase stability of MNCs can also be strongly altered as a result of this interplay. Three phase transformations are observed in cobalt ferrofluids for $T \sim 10$–300 K, namely second order magnetic phase transformations (blocked–unblocked transition) at the blocking temperature of the magnetic NP, first order magnetic and structural phase transformations at the solvent melting temperature, T_M, and second order premelting transformation at $T_{PM} < T < T_M$. These transformations show specific magnetic signatures in field-cool and zero-field-cool magnetization measurements and are qualitatively in agreement with predictions using M-spectrum theory.

(Some figures in this article are in colour only in the electronic version)

1. Introduction

Nanocomposites (NCs), defined as materials comprised of several distinct components with at least one component having characteristic dimensions at the nanometre scale, have attracted increasing interest in the last two decades due to their significant potential in practical applications as well as in fundamental research [1–4]. In general, nanosized objects dispersed in a bulk matrix can be broadly classified into three categories based on the dimensions of the nanosized components and the matrix; examples include, 0D nanoparticles (NPs) dispersed in a bulk matrix (a combination of zero-dimensional NPs and three-dimensional matrix, or 0–3 NC, in short, hereafter) [5]; 1D nanorods/nanowires/nanowhiskers in a bulk matrix (1–3 NC)

[1] Current address: Physics Department, Carnegie Mellon University, Pittsburgh, PA 15213, USA

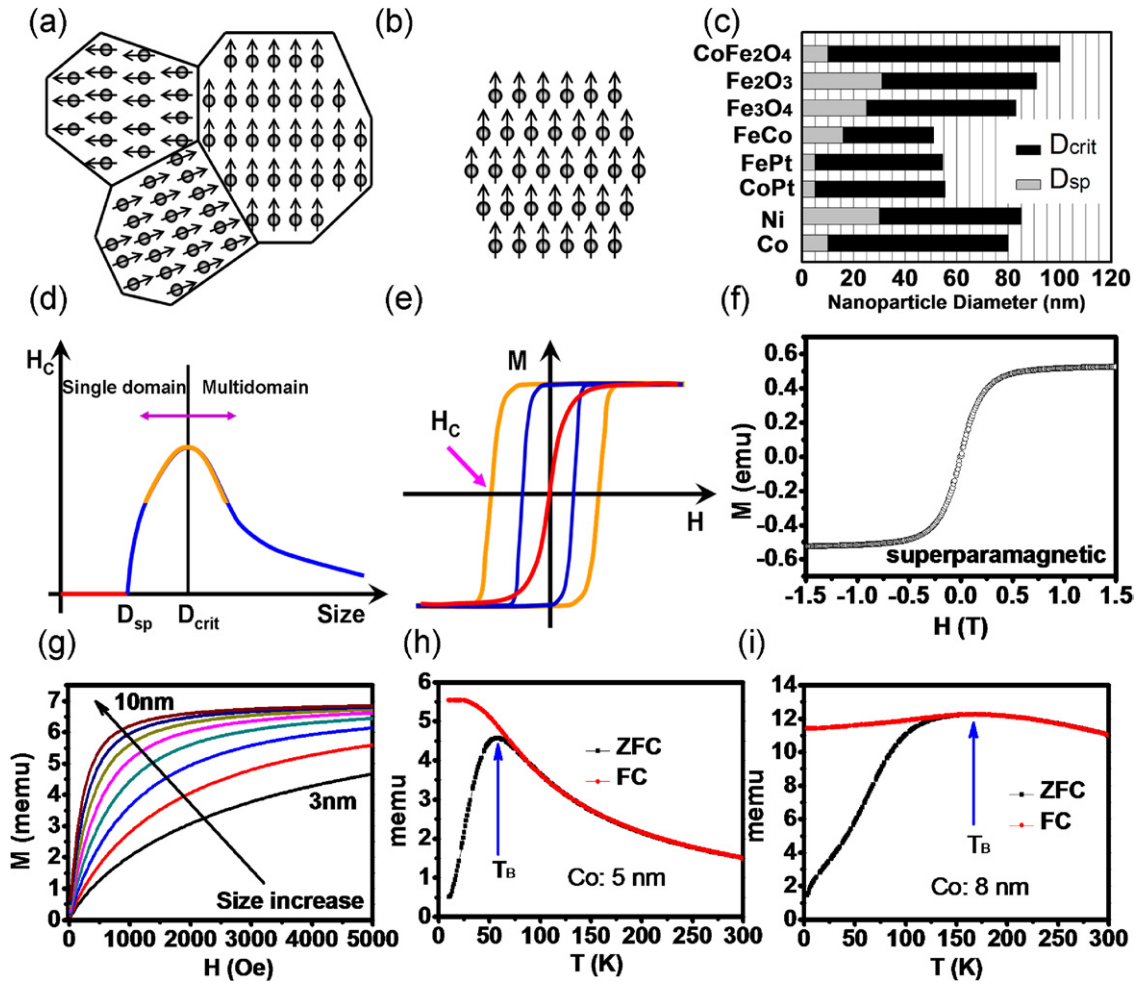

Figure 1. Schematic multiple and single magnetic domain structures for bulk and NPs in (*a*) and (*b*), respectively; each arrow represents the magnetic moment of an atom. Critical size of single domain and superparamagnetism of several materials in (*c*); (*d*) shows the coercivity of magnetic NPs and the corresponding hysteresis loops as a function of size in (*e*); closed hysteresis loop of superparamagnetic NPs at room temperature is shown in (*f*); (*g*) shows the size sensitive room temperature $M(H)$ curves (simulated) in steps of 1 nm; (*h*) and (*i*) show the zero field cooling/field cooling (ZFC/FC) curve of magnetic cobalt NPs with a mean size ∼5 nm and 8 nm, respectively, the temperature corresponding to the peak of the ZFC curve is defined as blocking temperature (T_B).

[6], and 2D nanosheets in a bulk matrix (2–3 NC) [7–9]. In addition to the bulk matrix, nanosized objects can be directly integrated with other nanosized components. For example, gold NP decorated zinc oxide nanowires, a 0–1 NC, show enhanced gas sensitivity to carbon monoxide at room temperature [10]. By controlling the radial and axial growth, epitaxial semiconductor core–shell nanowire heterostructures, a 1–1 NC, have also been successfully fabricated [11]. Most recently, a new category of NCs, namely 0–0 NC, has attracted much interest. These 0–0 NCs include core–shell [12–14] and dumbbell [15] morphologies. Overall, NCs can be engineered to have a variety of unique properties. By controlling the chemical composition, physical properties and morphology of the chosen components, it is possible to tune the physical properties of NCs across a wide spectrum, from mechanical [16, 17], optical [18, 19], thermal [20], to electrical [21], chemical [22] and magnetic properties. This broad spectrum of unique physical and chemical properties lends NCs to various applications from radiation sensors [23] to biomedicines [24].

Magnetic nanocomposites (MNCs), a typical combination of magnetic nanoparticles (MNPs) and another component, exhibit a wide range of novel properties associated with MNPs. First, MNPs can respond to an external magnetic field without physical contact, making them attractive for remote applications. Second, as the size of the MNPs shrinks from the bulk to the nanoscale, different magnetic properties, compared with their bulk counterparts, can be obtained. When particle size is smaller than a critical size, D_{crit}, as in figure 1(*c*), multi-domain magnetic structures in the bulk (figure 1(*a*)) will become single domain (figure 1(*b*)). In the vicinity of D_{crit}, the coercivity of MNPs is largest and will decrease as particle size decreases, until it reaches the superparamagnetic limit, D_{sp}, as defined in figure 1(*c*) for various materials, below which the coercivity is zero for all sizes at room temperature [25]. Superparamagnetism [26] is a unique property of single domain MNPs, and is determined by size, temperature and measurement time. At room temperature, and 100 s measurement time, particle sizes smaller than D_{sp} give closed magnetic hysteresis loop, as

shown in figure 1(*f*). Finally, and more intriguing, the properties of MNPs are tunable as a function of particle size, particle size distribution and interparticle interactions [27]. Even though the hysteresis loops are all closed for superparamagnetic NPs, their shapes are also sensitive to the size of MNPs, as shown in figure 1(*g*), with larger particles being more easily saturated at lower field. Although, dictated by the distributions of NP sizes and anisotropies as well as interparticle interactions in fine particle system, the peak observed in the zero field cooling (ZFC) measurement is often taken to be proportional to the blocking temperature. The relationship between the peak and the blocking temperature is not always linear, for samples with a wide distribution of energy barriers. However, for our synthesis in organic solvents, where the size distribution is very narrow, the peak is a good estimate for the mean temperature of the blocking transition for ensembles of MNPs. The peak in the ZFC curve, hereafter denoted by T_B, will also increase with particle size [28] and interparticle interaction [29], as shown in figure 1(*h*) and (*i*). In addition to these striking magnetic properties inherent in MNPs, MNCs also possess other advantages. For instance, the second component of the MNCs can sometimes acts as an excellent dispersant of MNPs [30] making them very attractive for real applications [31]. In addition, any unique properties of the second component can be combined with that of the MNPs for bi/multi-functional applications as in the 'two-in-one' magnetic-fluorescent MNC [32]. Further, synergic combination of the MNPs and the second parent phase could also lead to novel and new properties [33].

Morphologically, MNPs can combine with a second phase in several ways to make MNCs: MNPs can be dispersed in a solid matrix [34, 35], in a liquid matrix [36, 37], or combined with another nanoscale component [13, 15, 38]. Although some MNCs are fabricated by physical methods, for example cobalt or nickel NPs synthesized in a SiO_2 matrix by coevaporation [39], MNCs can be easily fabricated by wet-chemical methods with distinct advantages, such as easy-processability, low cost, controllable morphologies and size of MNPs. Significantly, synthesis in organic solvents produces a narrow size distribution of MNPs [40, 41, 167], which is of tremendous advantage for MNPs with relaxation time that depends exponentially on volume. For wet-chemical synthesis of MNCs, there are three different strategies, namely separate step synthesis, sequential step synthesis and simultaneous synthesis. For the separate step synthesis, MNPs and other components are prepared separately, followed by a simple mixing of the individual components [43]. For the sequential step synthesis, one component of the MNCs is synthesized first, and the second component is directly synthesized in the presence of the first component. This strategy is often employed to fabricate core–shell [13, 14, 38, 44] or dumbbell shaped nanostructured [15] as well as MNPs-polymer MNCs [45, 46]. For the simultaneous synthesis, MNPs and other components are produced at the same time, often with the aid of each other. This strategy has been used to fabricate the Ag/Co immiscible NPs [47].

Among the various ferromagnetic materials, cobalt MNP is a good choice for MNC applications. Cobalt MNPs with good magnetic properties can not only be easily synthesized by a well-established thermal decomposition method [40, 41, 167], but they also lend themselves to a wide range of self-assembling possibilities [48, 49]. As an oxide counterpart to cobalt MNPs for MNC applications, ferrimagnetic magnetite MNPs with uniform and tunable size can also be synthesized in organic solvents and stabilized by coating of surfactants [50–52]. Compared with cobalt MNPs, magnetite MNPs are 'inert' in terms of chemical stability, nontoxicity and thermal stability. Firstly, magnetite MNPs can be stable in air and in water for extended periods of time [53], while cobalt MNPs are 'active' in oxidizing environment, and can be easily oxidized to cobalt oxide NPs with the possibility to transform to hollow nanostructures by Kirkendall effects [54]. Secondly, magnetite MNPs are also non-toxic and thus desirable for applications in living bodies [24], while cobalt MNPs are very toxic for such applications. Thirdly, morphologies of magnetite MNPs are relatively stable at elevated temperature due to very limited diffusivity of ionic materials. As a result of their 'inert' nature, magnetite MNP-based MNCs are good candidates for applications in the presence of oxidizing environment. Typically, they are often chosen as agents for *in vivo* and *in vitro* biomedical applications [24], such as contrast agents for magnetic resonance imaging [55] (MRI), tracers for magnetic particle imaging [56] (MPI), drug delivery [57, 58] and hyperthermia [59–61]. Despite the fact that cobalt-based MNCs are unsuitable for *in vivo* applications, they excel in many aspects for inorganic applications due to their superior magnetic and electrical properties over magnetite MNPs. For example, cobalt MNPs with much higher magnetization can respond much more strongly to an external magnetic field gradient for remote applications. Further, much higher diffusivity of metallic cobalt atoms makes cobalt NP-based materials suitable for thermodynamic and kinetic investigations of atomic migration and associated morphological transformations at the scales of NPs. Finally, cobalt MNPs with better electrical conductivities make them a better choice for subtle magnetotransport investigations. Using cobalt MNPs as the basic constituent, we categorize and fabricate three distinct types of cobalt-based MNCs, as shown in figure 2, namely Au_{core}–Co_{shell} NPs (figure 2(*a*)), cobalt/polymer hybrid MNCs (figure 2(*b*)) and cobalt ferrofluid (FF) (figure 2(*c*)). Since both the core and shell are metal, Au_{core}–Co_{shell} composite NPs are called 'hard' NCs. Alternatively, due to the flexibility of the matrix, Co/polymer hybrid film is called 'soft' NCs. Finally, cobalt NPs dispersed in a solvent exhibit both translational and/or rotational diffusion, and are thus called 'dynamic' NCs.

Even though MNCs have been studied recently, many fundamental and critical problems, including thermal, electrical and magnetic properties, still need further investigation. In fact, each type of cobalt-based MNCs, identified above, were designed to address an important and specific attribute of MNCs. First, for the hard Au_{core}–Co_{shell} NCs, even though the components, Au and Co, are immiscible according to the bulk phase diagram [62], their stable MNC morphology depends on thermodynamic and kinetic factors. Diffusion, interface and surface

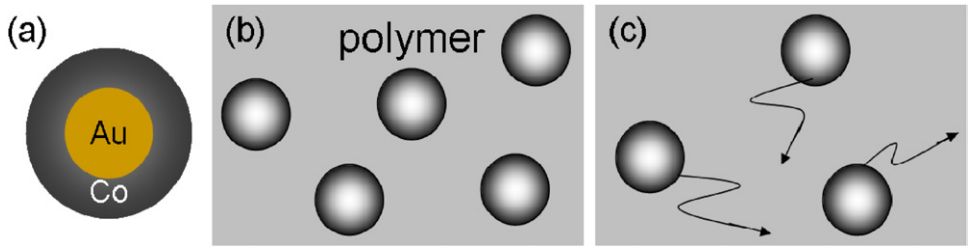

Figure 2. Three types of cobalt-based MNCs: (*a*) Au_{core}–Co_{shell} composite NPs; (*b*) Cobalt/polymer hybrid NCs; and (*c*) cobalt FFs in different organic solvents.

energies increasingly play an important role and the overall energy minimization can lead to surprising results in the equilibrium structure. Second, the dependence of the electrical resistance on external magnetic field has been observed in the ferromag/nonmag/ferromag multilayer structures [39, 63–66] as well as in related granular systems, in which MNPs are dispersed in a nonmagnetic metallic or conducting matrix. Further, semiconducting polymers have been widely explored recently in the application of electronics devices due to various advantages [67]. Inspired by semiconducting polymer electronics device, the nonmagnetic inorganic matrix in a granular magnetoresistance (MR) system can be replaced by an organic semiconducting polymer such as poly (3-hexylthiophene, 2,5-diyl) or P3HT. Electron transport and MR in such soft cobalt/P3HT hybrid MNCs, in which cobalt MNPs are dispersed in a P3HT matrix, has been studied. Finally, in cobalt FFs, a dynamic NC, two phase transitions—a second order magnetic phase transformation [68] (blocked-to-unblocked superparamagnetic transition) as well as a first order structural transformation (melting of the carrier solvent)—can be observed. The second order magnetic phase transformation at T_B can be tuned by the size and size distribution of cobalt NPs, and their interparticle interactions. The first order structural transformation at the melting temperature of solvent (T_M) can be varied by choosing a different solvent. By choosing the size of the cobalt NPs and the solvent properly, it is possible to couple the second order magnetic and the first order structural phase transformations ($T_M \sim T_B$). Here, we first describe the fabrication of these three types of cobalt-based MNCs, followed by details of each designated problem. Finally, conclusions will be drawn and the outlook for future research work on MNCs will be presented.

2. Cobalt-based MNCs

2.1. Synthesis of cobalt NPs

Cobalt MNPs can be synthesized by the well-established thermal decomposition method in the presence of surfactants [40]. The cobalt MNPs synthesized by this method are always coated with surfactants with hydrophobic tails to protect them from agglomeration and oxidation in organic solvents, as shown in figure 3(*b*). The bright field transmission electron microscopy (TEM) image of typical 9 nm spherical cobalt MNPs is shown in figure 3(*c*). Such chemically synthesized cobalt NPs are metastable with a crystalline structure not observed in the bulk, namely the so-called ε-phase of cobalt

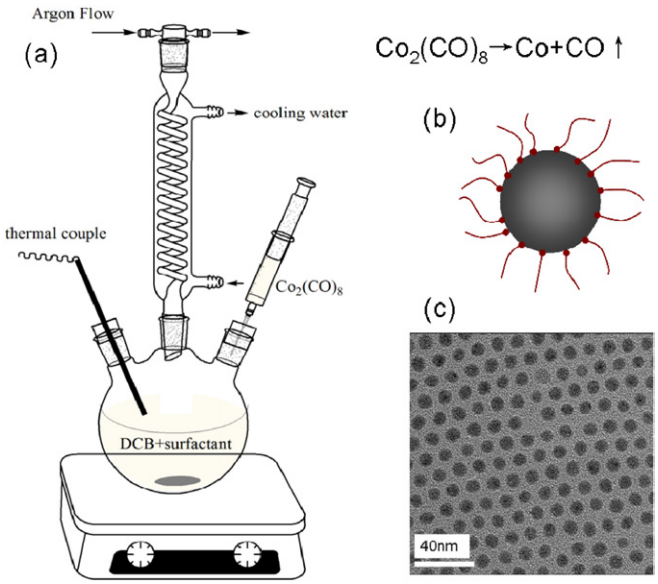

Figure 3. (*a*) A schematic of the Schlenk line where the cobalt NPs are synthesized; (*b*) the cartoon shows the cobalt NPs coated with surfactant; and (*c*) the bright field TEM image of synthesized cobalt NPs (9 nm). The interparticle separation is typically twice the surfactant chain length.

[69]. This crystalline structure has cubic symmetry (space group $P4_132$) with a β-Mn unit-cell structure [69], containing 20 cobalt atoms, and a large lattice parameter ($a_0 = 6.097$ Å) [69]. Further, the metastable crystal structure of ε-Co, unique only to the nanocrystals, transforms to hexagonal close packed (hcp) cobalt NPs at 300 °C and face centred cubic (fcc) cobalt at 500 °C, respectively [70]. In addition to spherical ε-Co NPs, hcp cobalt nanodiscs can also be fabricated with the same thermal decomposition procedure by choosing proper surfactants [71]. In practice, a pair of surfactants are used to fabricate spherical and monodispersed cobalt NPs [72, 73]. In a typical synthesis of spherical cobalt NPs, using oleic acid (OA) and dioctylamine (DOA) as example, the Schlenk line (figure 3(*a*)) is degassed for 30 min with argon; and then, 0.54 g $Co_2(CO)_8$ dissolved in 3 mL o-dichlorobenzene (DCB) is rapidly injected into 14 mL DCB with 0.2 mL OA and 0.34 mL DOA at 182 °C during vigorous stirring. Following burst nucleation and size focusing, cobalt NPs are collected after 20 min and sealed in vials filled with argon. As-made cobalt NPs in DCB are washed with ethanol, precipitated by centrifugation, dried in the vacuum, and finally dispersed in different solvents to make a wide range of FFs.

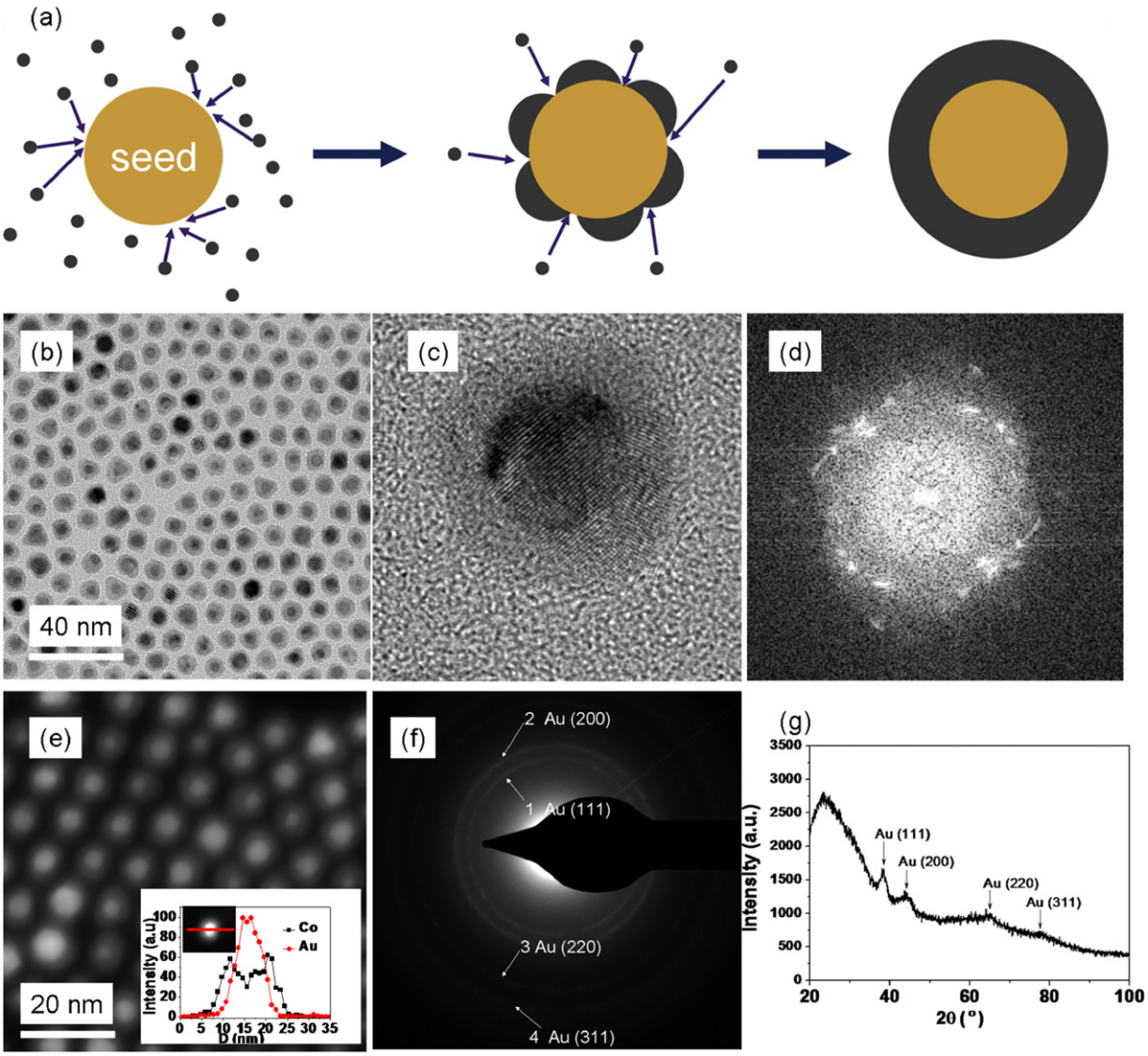

Figure 4. (*a*) Growth mechanism, (*b*) bright field TEM, (*c*) HRTEM and (*d*) corresponding FFT, (*e*) dark field STEM, (*f*) SAED and (*g*) θ–2θ XRD scan of Au_{core}–Co_{shell} NPs. The inset in (*e*) shows the EDX line scan with a probe size ∼1 nm in STEM mode.

2.2. Au_{core}–Co_{shell} *NPs*

Seed-mediated growth, a popular wet-chemical synthetic method to fabricate nanoscale heterostructures [74, 75], is used to fabricate core–shell NPs. Due to the lower activation energy of heterogeneous when compared with homogeneous nucleation, atoms in the supersaturated solution prefer to heterogeneously nucleate on the surface of the pre-fabricated seed NPs to yield core–shell NPs. The growth mechanism of Au_{core}–Co_{shell} NPs is schematically shown in figure 4(*a*). First, gold seed NPs are synthesized by a modified two phase Brust method [76]. Typically, 0.1 g $HAuCl_4$ dissolved in 6 mL D.I. water is stirred vigorously with 0.5 g tetraoctylammonium bromide (TOAB), a phase transfer agent, in 14 mL toluene for 3 h. Then 0.05 g dodecylamine (DDA) in 3 mL toluene is added to the above mixture, and stirred for another half an hour. During stirring, dodecylamine will coordinate to gold (III) ions. Finally, sodium borohydrate ($NaBH_4$), a strong reducing agent, in 6 mL D.I. water is added to the mixture/solution in a drop-wise fashion. Homogeneous nucleation of gold NPs is indicated by a quick colour change from milk white to blood red. The solution is kept stirring for another 3 h to complete the reaction. Gold NPs in the organic phase are then separated from the aqueous phase, and stored in a glass vial. As-made gold seed NPs solution also contains other by-products and residues, which are washed with methanol, precipitated by centrifugation, and dried in vacuum. After that, 0.05 g gold NPs are dissolved in 10 mL toluene, and subsequently transferred into the Schlenk line, followed by degassing with argon for 30 min. Gold seed NPs solution is then heated to 90°C and kept at this temperature for another 10 min. After that, 0.1 g $Co_2(CO)_8$ with 0.1 mL oleylamine (ON) and 0.1 g OA in 3 mL toluene is injected into the hot solution containing gold seed NPs. Upon decomposition, cobalt atoms heterogeneously nucleate on multiple positions on the surface of gold seed NPs as schematically shown in figure 4(*a*), and grow to become a complete shell. After 1 h, the solution was cooled down to room temperature, and collected and sealed in glass vials filled with argon, and stored in a glove box.

The bright field TEM image of Au_{core}–Co_{shell} NPs shows (figure 4(*b*)) gold cores appearing much darker than the cobalt shell. High resolution TEM (HRTEM) image of a Au_{core}–Co_{shell} NP, figure 4(*c*), shows that the spherical gold core is a single crystal surrounded by a polycrystalline cobalt shell. The fast Fourier transformation (FFT) of the HRTEM image in figure 4(*c*), as shown in figure 4(*d*), is irregular and confirms the multiple crystallographic orientations of the different grains in the cobalt shell. Au_{core}–Co_{shell} NPs were also characterized by dark field scanning TEM (STEM) with a probe size ∼1 nm and a high-angle annular dark field (HAADF) detector, which is sensitive to the atomic number (Z) and the thickness of the NPs. Gold and cobalt in the core–shell structure, with large difference in Z, are well resolved in the dark field STEM image in figure 4(*e*) exhibiting a brighter gold core and a darker cobalt shell. Energy dispersive x-ray (EDX) spectroscopy line scan in the STEM mode, across a Au_{core}–Co_{shell} NP is also shown in the inset of figure 4(*e*). The 'λ' and 'μ' shapes of gold and cobalt profile clearly indicate that the gold concentration is maximum at the centre, while cobalt is concentrated at the edge of Au_{core}–Co_{shell} NPs, respectively. Figure 4(*f*) shows the selected area electron diffraction (SAED) of Au_{core}–Co_{shell} NPs. The ring pattern can be assigned to the crystal plane (1 1 1), (2 0 0), (2 2 0) and (3 1 1) of the fcc gold core. The reduced intensity of the fcc gold diffraction ring can be attributed to the small size of the gold core and the screening effect by cobalt shell. Due to the small grain size in the multi-grained cobalt shell, no diffraction rings corresponding to cobalt can be indexed. Consistent with the SAED, the diffraction peaks in the θ–2θ XRD scan, shown in figure 4(*g*), can only be indexed as fcc gold, but no diffraction peaks attributed to cobalt can be observed. The characterization with bright field TEM, HRTEM, FFT, STEM and EDX confirms that Au_{core}–Co_{shell} NPs, with a single crystalline gold core and polycrystalline cobalt shell, were successfully fabricated. In addition, it has also been demonstrated that cobalt shells in Au_{core}–Co_{shell} NPs form single magnetic domains with enhanced coercivity, compared with pure cobalt NPs of the same size, as a result of pinning effect at the Au/Co interface [77].

2.3. Cobalt NPs/poly(3-hexylthiophene, 2,5-diyl) hybrid NCs

Poly(3-hexylthiophene, 2,5-diyl) (P3HT), a well-known semiconducting and semicrystalline polymer, has been widely used in organic electronics [78], such as transistors [79], photovoltaic devices [80] and diodes [81]. The conductivity of P3HT is 10^{-6}–10^{-7} S cm^{-1} for pressed pellet [82], and 10^{-8}–10^{-9} S cm^{-1} for cast film [83]. Due to the alkyl chain on each monomer, P3HT can be well-dissolved in any non-polar organic solvent, making it very easy for solution processing. In solution, the polymer chains of P3HT are uniformly dispersed, as schematically shown in figure 5(*a*). However, upon solvent evaporation, due to its regioregular structure, polymer chains of P3HT usually crystallize into laminar crystallites interspaced by amorphous regions [78, 84] (figure 5(*f*)). Figure 5(*a*) shows the steps to fabricate Cobalt NPs/P3HT (Co/P3HT) hybrid thin films by drop casting. In step I, as-made cobalt MNPs are washed with ethanol, precipitated by centrifugation and dried in vacuum. Depending on the desired volume ratio of cobalt MNPs to P3HT, various amounts of P3HT are co-dissolved with dried cobalt MNPs in toluene. In each batch of precursor solution, concentration of P3HT is 10 mg/1 mL. The co-dissolved Co/P3HT solution in toluene is sonicated for 2 h to form a homogeneous solution. In step II, a drop of the prepared Co/P3HT solution (63 μL) is cast on the substrate, which becomes the Co/P3HT hybrid film after toluene is evaporated, as in step III. Finally, in step IV, the cast Co/P3HT hybrid film is annealed in a flow of 5 vol% H_2/95 vol% Ar atmosphere at 150 °C for two hours. The annealing temperature is determined based upon the thermal gravimetric analysis (TGA), as shown in figure 5(*b*). During annealing, the residual solvent is evaporated completely, and then the cobalt NPs and P3HT form a stable configuration.

Regioregular P3HT often crystallizes into a semicrystalline laminar structure with a lattice parameter, $a_0 = 1.61$ nm and $b_0 = 0.38$ nm [85]. According to Bragg's law, $2d_{hkl}\sin\theta = n\lambda$, coherent x-ray scattering along the (1 0 0) and (0 1 0) direction will occur at 5.4° and 23.4° with Cu K_α radiation ($\lambda = 0.154$ nm) [85]. Further, it has been demonstrated that there are two possible orientations of P3HT crystallites with respect to the substrate for the solution processed films [78]. For P3HT with high regioregularity, the planes of the P3HT sheets in the crystallites prefer to be perpendicular to the substrate (perpendicular configuration); while for the P3HT with low regioregularity, the planes of the P3HT sheet in the crystallites prefer to be parallel to the substrate (parallel configuration). For the perpendicular configuration, θ–2θ x-ray scans will show peaks at 5.4° for the (1 0 0) plane, 10.8° for the (2 0 0) plane and 16.2° for the (3 0 0) plane; while for parallel configuration, the peak will only appear at 23.4° for the (0 1 0) or (0 0 1) planes. The XRD θ–2θ scans of pure cobalt NPs, pure P3HT and their MNCs using Cu K_α radiation are shown in figure 5(*c*). The diffraction peak at 44.2° for pure cobalt NPs confirms the ε-Co crystallographic structure. For pure P3HT, there are three strong diffraction peaks located at 5.4°, 10.8° and 16° corresponding to the (1 0 0), (2 0 0) and (3 0 0) reflections, respectively. The strong (1 0 0) peak at 5.4° has been truncated to reveal the details of the XRD pattern of pure P3HT. The broad peak of the pure P3HT with maximum at ∼23° might be due to a small number of crystallites with parallel configuration, which is consistent with other observation [86]. The diffraction pattern of pure P3HT indicates that the drop casted P3HT prefers the perpendicular configurations.

When cobalt NPs are added to P3HT to form the MNCs, the diffraction intensity of P3HT at $2\theta = 5.4°$, 10.8° and 16° is considerably reduced as shown in figure 5(*c*). The peak intensity of P3HT at $2\theta = 5.4°$ is proportional either to the total number of nanodomains of crystalline P3HT per unit volume [85] or to the fraction of the domains with *a*-axis oriented normal to the substrate surface [78]. As a result, the reduced diffraction intensity at $2\theta = 5.4°$ can be attributed to either reduced number or the reorientation of existing P3HT crystallites after addition of cobalt NPs. If the latter is the case, the diffraction peak of the (0 1 0) and (0 0 1) planes at 23.4° should increase. However, no diffraction peak at $2\theta = 23.4°$ was observed for Co/P3HT

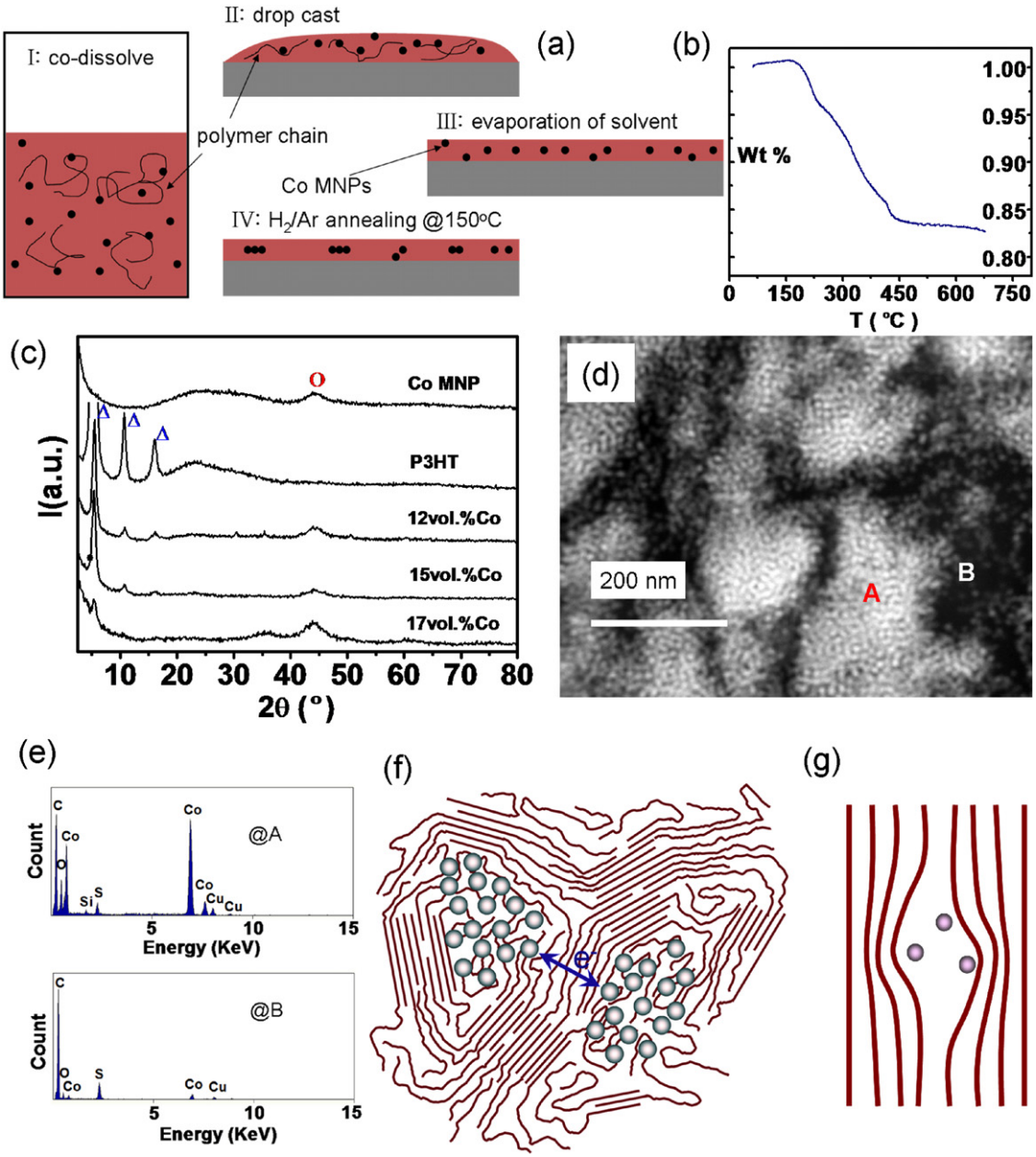

Figure 5. (*a*) Schematic steps to fabricate Co/P3HT soft NCs with its TGA measurement in (*b*). The x-ray θ–2θ scan using Cu Kα radiation of Co MNPs, P3HT and Co/P3HT hybrid films in (*c*); (*d*) shows the STEM image of sliced Co/P3HT hybrid film, and EDX analysis at points A and B in (*d*) is shown in (*e*); (*f*) shows the schematic microstructure of Co/P3HT hybrid films. Co NPs stays in the amorphous region of P3HT, because insertion of Co NPs into the crystalline region of P3HT, as shown in (*g*), will distort the laminar structure of P3HT to increase free energy.

MNCs. Hence, we can conclude that the addition of cobalt NPs into P3HT will reduce the number of P3HT crystallites per unit volume. Further, the diffraction intensity of P3HT (1 0 0) plane at $2\theta = 5.4^\circ$ decreases as the concentration of cobalt NPs in the P3HT matrix increases. Consequently, it is proposed [87] that cobalt NPs stay in the amorphous region of P3HT to form clusters (figure 5(*f*)) rather than be uniformly dispersed in the P3HT matrix (figure 6(*d*)). If cobalt NPs are inserted into the crystalline region of P3HT, the laminar structure will be distorted and strained, which is an unfavourable energy state [88]. Further, as more cobalt NPs are added to the P3HT matrix, some P3HT chains in the lamina will unfold and become amorphous to accommodate the cobalt NPs. As a result, the intensity of the diffraction peak at $2\theta = 5.4^\circ$ is inversely proportional to the volume concentration of cobalt NPs in the P3HT matrix. To confirm the proposed microstructure of Co/P3HT MNCs, direct imaging of sliced Co/P3HT thin films were conducted by dark field STEM, as shown in figure 5(*d*). Due to the larger atomic number (Z) of cobalt when compared with the average Z of P3HT, the region containing cobalt NPs appears brighter than the P3HT region. From the STEM image, it is clearly resolved that cobalt NPs are clustered (bright regions) and are separated by the P3HT matrix (dark region). The chemical compositions

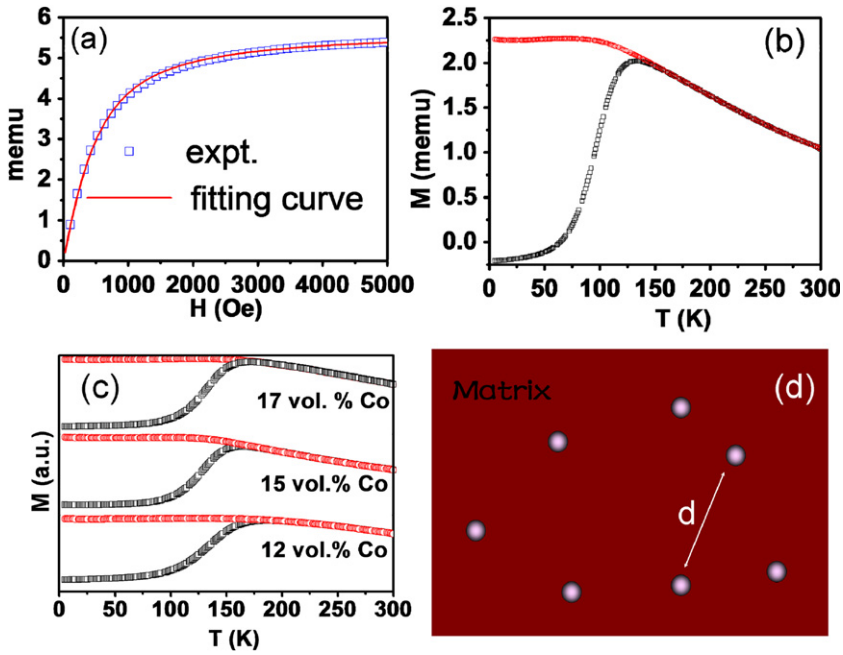

Figure 6. Chantrell fitting of the $M(H)$ curve for 15 vol% Co/P3HT NC in (*a*); ZFC/FC curve of the unannealed 15 vol% Co/P3HT in (*b*) and annealed Co/P3HT NC in (*c*); and uniform distribution of NPs in matrix (*d*)

are also confirmed by EDX spectra taken at point A and point B with an electron probe size of diameter ∼1 nm as shown in figure 5(*e*). The main components at point A are cobalt NPs and P3HT, while only strong peaks from P3HT can be observed at point B. In summary, the Co/P3HT MNCs show a segregated microstructure, which has to be incorporated in any model explaining the transport properties (see section 4.1).

$M(H)$ curves of Co/P3HT MNC shows superparamagnetic characteristics, and were fitted to a Langevin function using the Chantrell's method and assuming log normal size distributions [89, 90], as shown in figure 6(*a*). The magnetic size, d_m, of cobalt NPs in the Co/P3HT MNCs extracted from the fitting is $d_m \sim 7.6$ nm with a standard deviation of 0.6 nm, which is consistent with the physical size of cobalt MNPs, $d_o \sim 8$ nm, determined by bright field TEM. The small difference between d_m and d_o might be due to the magnetic dead layer on the surface of the cobalt NPs [91]. ZFC and FC curves of unannealed and annealed Co/P3HT MNCs are shown in figure 6(*b*) and (*c*), from which T_B is determined to be ∼125 K and ∼175 K, respectively. The shift of T_B is attributed to the redistribution of cobalt NPs during annealing, leading to stronger interparticle interactions. Further, after annealing, the T_B of Co/P3HT MNCs becomes insensitive to the concentration of cobalt NPs in the P3HT matrix (figure 6(*c*)), which results from the clustered microstructures of Co/P3HT MNCs, as shown in figure 5(*f*). The average interparticle spacing of the cobalt NPs clusters in the P3HT matrix is independent of the concentration of cobalt NPs, leading to approximately the same T_B (interparticle interactions) of all Co/P3HT MNCs. Further, if cobalt NPs are uniformly distributed in the P3HT matrix as shown in figure 6(*d*), T_B will increase with the concentration of cobalt MNPs due to enhanced interparticle interaction, which is not observed experimentally and thus magnetically prove the segregated microstructure of Co/P3HT hybrid films.

3. Thermal stability of Au_{core}–Co_{shell} hard NCs

Bi-/multi-functional, 0–0 type, MNCs [92, 93] have shown great potential to succeed in such applications as biomedicine [24, 94] and permanent magnets [95]. Hence, it is critical to have a comprehensive understanding about the fundamental and underlying properties of these 0–0 type MNCs. For example, the thermal stability of such 0–0 type MNCs could be significantly affected by surfaces [96] and interfaces [97] at the nanoscale, and the strain energy stored in the bulk due to lattice distortion [98]. In effect, the break in symmetry at newly created surfaces or interfaces introduces extra energy and entropy terms into the free energy of nanoscale materials, and thus alters their thermal properties [99–102]. Here, we discuss annealing experiments carried out on immiscible Au_{core}–Co_{shell} NPs to investigate their thermal stability, and specifically to determine the role of various energies (surface, interface, grain boundary and strain) in their thermal behaviour and stable morphology of each isolated core–shell NC.

3.1. Energies in Au_{core}–Co_{shell} *NPs*

Due to the high surface-to-volume ratio for nanoscale materials, surfaces and interfaces are abundant in Au_{core}–Co_{shell} NPs. Basically, there are three types of interfaces in the solid phase [104]; namely type I: free surface, where atoms are exposed to vapour phase; type II: intraphase interface (or grain boundary), where the phases are the same on both sides of the boundary but with different crystal orientations; and type III: interphase interface, where the phases are different on each side of the boundary. Here, phases refer to crystallites with fixed chemical composition and well-defined crystal structures. Compared with atoms in the bulk, the atoms at the interface have higher energy due to reduced symmetry.

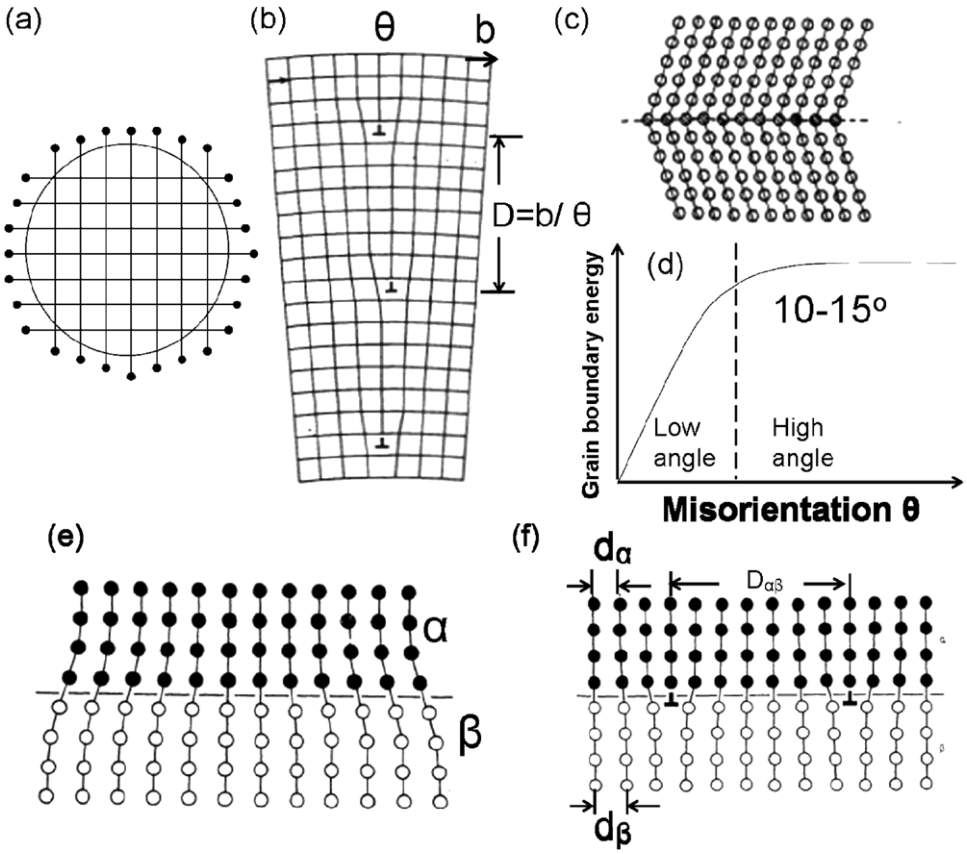

Figure 7. (*a*) Dangling bonds at the surface; (*b*) small-angle grain boundary with dislocations (after [103]); (*c*) twin boundary; (*d*) grain boundary energy as a function of misorientation angle; (*e*) coherent and (*f*) semi-coherent interface (figures adapted from [104]), copyright (1992) by Taylor and Francis, reprinted with permission.

With respect to atoms in the bulk, surface atoms (type I interface) partially lose their neighbouring atomic coordination (figure 7(*a*)) to yield a high-energy state. On the other hand, when solids are sublimated, atoms will lose all their neighbouring atoms. As a result, surface energy can be estimated by the latent heat of sublimation, L_S. If closest atomic packing is assumed, surface energy, γ_S, can be estimated from latent heat of sublimation as follows [104]:

$$\gamma_S = aL_S/N_A \text{ J/surface atom} \tag{3.1.1}$$

where N_A is Avogadro's constant, and the coefficient a (<1) is a crystallographic orientation (atomic packing) dependent parameter. For type II interface (grain boundary), there are two possibilities. When the misorientation angle, θ, between the crystallites on each side of the boundary is small, a small-angle grain boundary can be obtained as shown in figure 7(*b*). In this case, edge dislocations will be present at the interface with a dislocation distance of $D = b/\theta$ (b is burger's vector of the dislocation); i.e. the dislocation density is proportional to θ. As a result, the energy of a small-angle grain boundary, γ_b, is equal to the dislocation energy per unit area, and is linearly dependent [104] on θ, namely $\gamma_b \propto \theta$. As θ become large, dislocations at the grain boundary cannot be individually separated, and will form clusters of dislocation. For $\theta > 10°$–$15°$, the grain boundary will become disordered, and is called random high-angle grain boundary with energy levelled-off to one third of the free surface value, given in equation (3.1.1), i.e.

$$\gamma_b = \tfrac{1}{3}\gamma_S. \tag{3.1.2}$$

In a special high-angle grain boundary (twin boundary), as shown in figure 7(*c*), the grain boundary energy is often very low due to the absence of the dislocations and minimal distortion of the lattices on opposing sides of the grain boundary.

For type III interface, there are three possibilities, namely coherent, semi-coherent and incoherent interface [104]. Figure 7 shows the coherent (*e*) and semi-coherent (*f*) interfaces between α and β phases with lattice spacing d_α and d_β, respectively. At the coherent interface, atoms of phase α and β have one-to-one correspondence. However, chemical bonds at the interface are formed between atoms of different elements. Hence, interface energy, $\gamma_{\alpha\beta}$, is mainly attributed to chemical mismatch, i.e.

$$\gamma_{\alpha\beta} = \gamma_{\text{chem}} \tag{3.1.3}$$

which is usually very small (~1–200 mJ m^{-2}). If the lattice mismatch is significant between phase α and β, lattice distortion will be too strong to support a coherent interface. In this case, misfit dislocations (figure 7(*f*)) will be introduced at the interface to form a semi-coherent interface and to contribute to $\gamma_{\alpha\beta}$. The misfit factor between the two lattices is defined by

$$\delta = (d_\beta - d_\alpha)/d_\alpha. \tag{3.1.4}$$

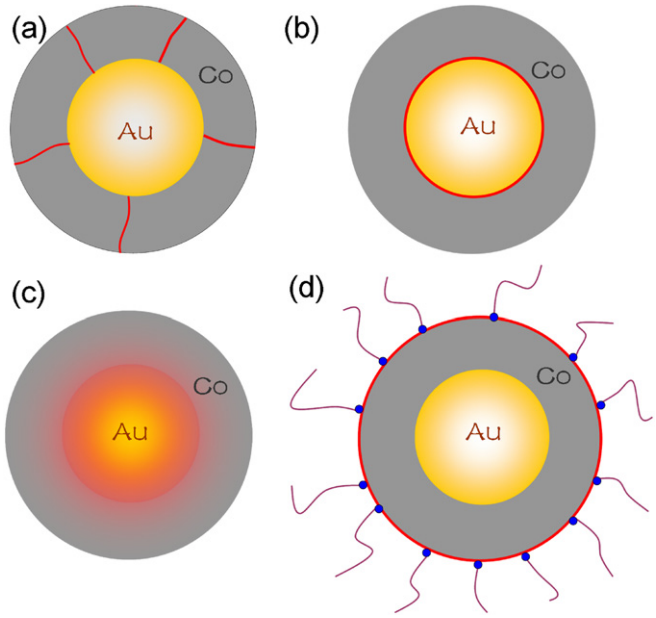

Figure 8. Energies in the Au_{core}–Co_{shell} NPs: (*a*) grain boundary energy in the cobalt shell; (*b*) the interfacial energy at the gold/cobalt interface; (*c*) strain energy stored in the bulk of both gold core and cobalt shell; and (*d*) the surface energy at the interface between the functional group of surfactant and the surface atoms of Au_{core}–Co_{shell} NPs. Each energy is highlighted by red.

The distance between misfit dislocations is given by (figure 7(*f*))

$$D = d_\beta/\delta \approx b/\delta \tag{3.1.5}$$

where b is the Burgers vector of the dislocations, and is given by $b = (d_\alpha + d_\beta)/2$. For a semi-coherent interface, the interface energy has contributions from both the chemical mismatch and the misfit dislocations, γ_{misfit},

$$\gamma_{\alpha\beta} = \gamma_{chem} + \gamma_{misfit}.$$

For a small misfit factor, the contribution from the misfit dislocation is proportional to misfit factors, namely

$$\gamma_{misfit} \propto \delta. \tag{3.1.6}$$

The energy of a semi-coherent interface is usually between 200 and 500 mJ m^{-2}. Finally, as the misfit factor δ is very large, the interface is not semi-coherent any more, and becomes a disordered interface with significantly enhanced interface energy $\gamma_{\alpha\beta}$ (∼500–1000 mJ m^{-2}) [104].

A chemically synthesized Au_{core}–Co_{shell} NP has a single crystalline gold core surrounded by a multi-grained cobalt shell due to heterogeneous nucleation. In such Au_{core}–Co_{shell} NP, there is unrelaxed grain boundary energy stored at the interface (type II) between cobalt grains in the shell, as shown in figure 8(*a*). In addition, extra energy is also stored at the interface between the gold core and cobalt shell. Ideally, the lattices of the gold core and the cobalt shell should be coherent so that energy is minimized at the interface. However, for as-made Au_{core}–Co_{shell} NPs, the interface between gold and cobalt is often incoherent due to random cobalt crystal growth on gold during heterogeneous nucleation to yield a high-energy state, as shown in figure 8(*b*). The average energy of the bare gold and cobalt surface [105] is 1.626 J m^{-2} and 2.709 J m^{-2}, respectively, with respect to the undistorted bulk atoms. In reality, as-made Au_{core}–Co_{shell} NPs are always coated with a layer of surfactant to prevent oxidation and aggregation, as shown in figure 8(*d*). Effective coating of any surfactant on the surface of metallic NPs is achieved by coordination bonds between surface atoms of the NPs and functional groups of the surfactants, which are covalent in nature and are formed by donating or accepting a pair of electrons from the functional groups into the empty orbital of surface atoms. Due to the strong bond strength of the coordination bonds, energy of the surface atoms is significantly reduced. If the interface between the surfactant/surface is considered as the 'surface' of Au_{core}–Co_{shell} NPs, 'surface' energy of these Au_{core}–Co_{shell} NPs is negligibly small or even negative. As a result, when considering the thermal stability in the Au_{core}–Co_{shell} NPs, 'surface' energy of the Au_{core}–Co_{shell} NPs can be neglected.

Finally, due to lattice mismatch, the lattices in both the gold core and the cobalt shell will be distorted, giving rise to strain energy in the bulk of Au_{core}–Co_{shell} NPs with respect to the unstrained lattice, as shown figure 8(*c*). The magnitude of the strain energy density in the uniformly deformed lattice is proportional to the product of Young's modulus and the square of the strain, defined as $\varepsilon = (d_{hkl} - d^*_{hkl})/d^*_{hkl}$, where d_{hkl} and d^*_{hkl} are the lattice spacing in the strained and unstrained lattice in any crystallographic direction [h k l], respectively. To calculate the strain energy in a Au_{core}–Co_{shell} NP, Eshelby's inclusion model, namely a spherical particle in an infinite matrix [106], is used. In this model, J D Eshelby performed a series of sequential virtual operations, namely cutting, straining and welding. By these virtual operations, the total strain energy stored in the spherical particles and the infinite matrix was calculated and given by

$$E_S = 2\mu V\varepsilon^2(1+\sigma)/9(1-\sigma) \tag{3.1.7}$$

where μ, ε, σ and V are the shear modulus, strain, Poisson's ratio and volume of the core, respectively. Strain energy is mainly concentrated in the vicinity of the interface between the spherical particle and the matrix, and the strain energy will quickly diminish when it is away from the interface. The total strain energy of the Au_{core}–Co_{shell} NPs thus can be estimated by equation (3.1.7) with limited errors. Accurate calculation of strain distribution in the core–shell NPs is performed by Duan *et al* [107]. In summary, the principal energy contributions to determine the stability of the particles include grain boundary energy in the cobalt shell, interface energy at the Au/Co interface and strain energy in both gold core and cobalt shell.

3.2. Ex situ annealing and thermal stability of Au_{core}–Co_{shell} *NPs*

To study thermal stability of Au_{core}–Co_{shell} NPs, *ex situ* annealing experiments were performed on the as-synthesized Au_{core}–Co_{shell} NPs under argon atmosphere over a wide temperature range from 200 to 450 °C. First, a small drop of the toluene solution containing as-made Au_{core}–Co_{shell} NPs was deposited on a carbon film (thickness ∼ 20 nm) mounted on a copper grid. After the deposited carbon film was completely

dried, the TEM grid was annealed, after initial purging with Ar gas for 2 h, for 10 h at the desired temperature and then slowly cooled in Ar gas to room temperature. Au_{core}–Co_{shell} NPs were then annealed at 200 °C, 250 °C, 300 °C, 350 °C, 400 °C and 450 °C, respectively. For annealing temperatures higher than or equal to 450 °C, the carbon film was broken and folded so that only blurred TEM pictures could be obtained.

The choice of the carbon film for the *ex situ* heating experiment was based on the binary phase diagrams of gold/cobalt and carbon. Cobalt and carbon are completely immiscible below 422 °C; and only a limited solubility can be observed between 422 and 600 °C. Other substrates commonly used for TEM experiments, such as Si_3N_4 or SiO_x, contain silicon, and the possibility of forming several intermediate compounds between cobalt and silicon precluded their use in heating experiments of Au_{core}–Co_{shell} NPs. Binary phase diagrams of Au/Co–Ti and Au/Co–Mo were also examined for other possible choices of the TEM substrates. In these phase diagrams, intermediate compounds are always present. Consequently, carbon film is the best choice for these *ex situ* heating experiments. After *ex situ* heating experiments, the annealed Au_{core}–Co_{shell} NPs on the carbon film were taken out from the annealing chamber and transferred into a FEI Tecnai G2 F20 microscope operating at 200 kV with a field emission gun. The annealed Au_{core}–Co_{shell} NPs were characterized by bright field TEM, SAED, HRTEM, STEM and EDX to monitor their structural and morphological evolution during *ex situ* annealing at different temperatures.

Prior to the annealing, no oxidation was detected for the as-synthesized Au_{core}–Co_{shell} NPs either by SAED and EDX. Further, the furnace tube, where the annealing experiments were carried out, was carefully degassed with argon gas flow for 2 h to ensure no oxidation of cobalt metal occured during heating/annealing. However, it is well known that surfactants on the surface of the Au_{core}–Co_{shell} NPs will decompose/evaporate [108] during heating at high temperature for 10 h to leave exposed metallic surfaces [109]. Further, decomposition/evaporation of surfactants outside the Au_{core}–Co_{shell} NPs becomes more severe as annealing temperature goes higher. As a result, cobalt metal in the Au_{core}–Co_{shell} NPs can be quickly oxidized even at room temperature due to insufficient protection, whilst being transferred from the annealing chamber to the TEM machine. Despite the appearance of such oxidation, it should be emphasized that the oxidation of cobalt metal occurs when being transferred from the annealing chamber to the TEM chamber rather than during the *ex situ* annealing experiment. Further, oxidation during transfer will quickly quench the morphologies of the annealed Au_{core}–Co_{shell} NPs due to the very limited diffusion in the ionic materials [86]. As a result, morphologies of the heat treated Au_{core}–Co_{shell} NPs are unchanged and can be used to monitor the morphological evolution during annealing in spite of the occurrence of oxidation during transferring [168].

HRTEM images of annealed Au_{core}–Co_{shell} NPs are shown in figure 9. along with their corresponding FFTs (insets). The core–shell morphology is still preserved for $T_{anneal} = 250$ °C as shown in figure 9(*a*). Compared with the irregular FFT pattern of as-made Au_{core}–Co_{shell} NPs shown in figure 4(*d*), FFT pattern of the annealed Au_{core}–Co_{shell} NPs at $T_{anneal} = 250$ °C for 10 h is much more regular indicating that the grain boundaries in the cobalt shell are slowly annealed away by grain growth. Further, during annealing, the lattices of gold and cobalt are reoriented and aligned along the same direction to achieve a coherent or semi-coherent interface. After annealing at $T_{anneal} = 300$ °C for 10 h, FFT patterns of Au_{core}–Co_{shell} NPs become completely regular (figure 9(*b*)), indicating all cobalt grain boundaries have been annealed away, and the lattices of gold and cobalt are completely aligned. As Au_{core}–Co_{shell} NPs were annealed at 350 °C for 10 h, the gold core begins to escape from the containment of the cobalt shell, as shown in figure 9(*c*). Finally, after annealing at $T_{anneal} = 400$ °C for 10 h, gold and cobalt were transformed into a stable peanut structure as shown in figure 9(*d*). It is worth mentioning that even during the movement of the gold core out from the containment of the cobalt shell, the lattices of gold and cobalt remain coherent, as monitored by their corresponding FFTs. A low energy, twinned Co/Au interface, seen in the peanut structure in figure 9(*d*), is magnified in figure 9(*e*). Further, the whole process of the morphological transformation is recorded by bright field TEM images, and the morphologies are confirmed by the corresponding EDX line scan in the inset in figure 9(*f*)–(*i*).

As-made Au_{core}–Co_{shell} NPs are in a high-energy state with extra energy contributions from Co/Co grain boundary, Au/Co interface and strains in the lattices of gold and cobalt. At room temperature, the core–shell morphology, even at a high-energy state, is well preserved due to the limited mobility of gold and cobalt atoms. However, during annealing, atoms in the Au_{core}–Co_{shell} NPs will gain enough thermal energy to migrate so that the extra energy in the core–shell morphologies can be slowly relaxed. Initially, after annealing at 250 °C for 10 h, grain boundaries in cobalt shell are annealed out. Such grain growth at intermediate temperature is driven by the grain boundary enthalpy and the enhanced grain boundary mobility due to non-equilibrium grain boundary structures in nanocrystalline materials [111, 112]. The grain boundary energy is dependent on the misorientation angle, and can be as high as one third of the surface energy for a completely disordered grain boundary. Further, the shapes of the cobalt grains are random and are not in the equilibrium hexagonal shape [104, 111, 112]. As a result, the grain boundary will be annealed out easily even at temperatures as low as 250 °C. After annealing at 300 °C for 10 h, the free energy of the Au_{core}–Co_{shell} NPs can be further reduced by forming a coherent or semi-coherent interface. Although details of the structure of the Au_{core}–Co_{shell} NPs changes for $T_{anneal} = 300$ °C, the core–shell morphology remains intact. The coalescence is not severe as shown in figure 9(*f*). Further, after annealing at $T_{anneal} = 350$ °C for 10 h, gold cores gradually escape from the containment of the cobalt shell such that strain and interface energy will be reduced. Interface and strain energy will be minimized when the peanut structure is finally obtained after annealing at $T_{anneal} = 400$ °C for 10 h.

In summary, Au_{core}–Co_{shell} NPs follow a sequence of thermal transformations during annealing to minimize their total energy: (1) when thermal energy is low (<200 °C), the

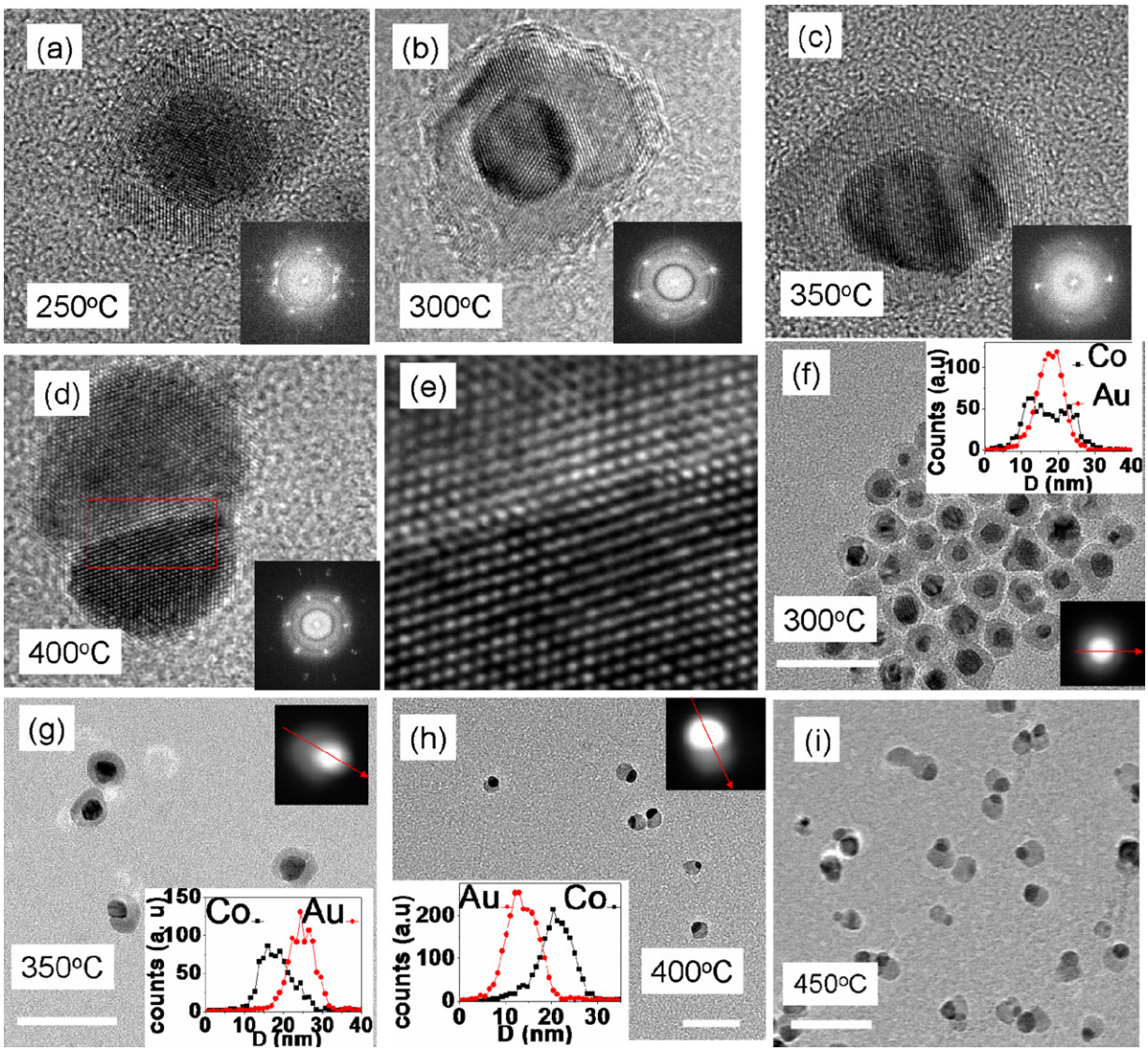

Figure 9. HRTEM of Au_{core}–Co_{shell} NPs annealed at 250 °C in (*a*), 300 °C in (*b*), 350 °C in (*c*) and 400 °C in (*d*); the FFT of each individual particle is shown as insets. The interface enclosed by the red rectangular area in (*d*) is magnified and shown in (*e*). The bright field TEM image of Au–Co NPs annealed at 300 °C in (*f*), 350 °C in (*g*), 400 °C in (*h*) and 450 °C in (*i*), the scale bar is 40 nm. The insets in (*f*)–(*h*) show the corresponding STEM image of annealed Au_{core}–Co_{shell} NPs, and the associated EDX line scans with probe size ∼1 nm.

core–shell morphology remains stable. (2) As the temperature increases (200–300 °C), cobalt atoms in the shell begin to diffuse, re-organize and eliminate the grain boundaries. Further, the gold and cobalt lattices re-orient and align to create a coherent/semi-coherent interface. (3) As the annealing temperature is further increased to 350 °C, atoms migrate more vigorously and the gold core begins to move out from being contained by the cobalt shell. This reduces the interfacial energy by diminishing the contact area and partially releases the strain energy as well. (4) Finally, strain, interface and grain boundary energies are minimized to form the 'peanut' structure for particles heat treated at 400 °C for 10 h [109].

4. Electron transport and MR in Co/P3HT soft NCs

Electron transport in disordered system via localized electronic states has been investigated in non-crystalline condensed materials for some time [113]. In practice, it is becoming increasingly important, partially due to the appearance of novel and new organic electronic devices [67, 113–118], with several advantages over their inorganic counterparts, in easy-processability [119], low cost, light-weight and flexibility [120]. Further, the transport of polarized spins in the presence of magnetic entities, in a structurally disordered polymeric MNCs system, is even more intriguing and needs further investigation. Organic materials (polymer or small molecules), enabling recent advances in organic electronics, is a new viable alternative for spintronics applications [121], mainly due to their weak spin–orbit and hyperfine interactions [121–124]. The pioneering work of organic spintronics was conducted in tunnel junctions using an organic spacer [125], a conjugated small molecule, tris(8-hydroxyquinolinato) aluminum (Alq_3), sandwiched by a half-metallic ferromagnet $La_{0.67}Sr_{0.33}MnO_3$ (LSMO) and a metallic ferromagnet (Co) to form a LSMO/Alq_3/Co tunnelling

junctions. Magnetoresistance (MR) ratio of ∼40% was observed at 11 K, which rapidly decreased to zero above 200 K. Later on, a room temperature TMR effect was demonstrated in the Co/Al_2O_3/Alq_3/NiFe tunnelling junction [126] with a room temperature MR ratio of ∼4%. Analogous to inorganic spintronics, MR can be observed in FM1/organic semiconductor/FM2 heterostructures as well as in the granular systems, in which single domain MNPs are dispersed in an organic matrix. Granular NC films comprised of cobalt NPs and small molecules have been fabricated by co-deposition. In these organic granular films, small molecules, such as C_{60} [127] and Alq_3 [128], form the organic matrix in which cobalt NPs are embedded. MR ratio of 80% and 12% was observed for the Co/C_{60} [127] and Co/Alq_3 [128] hybrid films at 4.2 K respectively, even though the electron transport mechanism and microstructure in these hybrid granular systems are still not clear. Here, we discuss electron transport and MR of granular Co/P3HT hybrid films synthesized by a totally different and inexpensive solution approach. Instead of small molecules, polymers are used as the matrix. Further, since P3HT matrix is a flexible polymer, this hybrid MNCs can potentially be a good candidate for a structurally flexible MR device, which is not achievable by tunnel junctions as well as by small molecule granular systems. Finally, the electron transport mechanism in the Co/P3HT hybrid MNCs is elucidated.

4.1. Electron transport in Co/P3HT soft NC

According to Bloch theorem [129], the wave function of electrons in a periodic potential is given by

$$\psi_k(r) = e^{ik\cdot r} \cdot u_k(r) \tag{4.1.1}$$

where $u_k(r)$ is a reflection of the period of the crystal lattice. In perfect crystals, the wave functions of electrons are periodic and can extend over the whole lattice of the material. In reality, there are always some imperfections in the crystalline material, leading to the loss of coherence of the Bloch wavefunction over a characteristic length scale, l; however, the electron wave can extend over the whole sample, as shown in figure 10(a). On the other hand, when the system becomes very disordered, the Bloch wavefunction will completely lose its coherence and become localized [130] as shown in figure 10(b), where ξ is the localization length [113].

The electron transport in a disordered system, in the classic Mott model, is via a phonon-assisted hopping process between these localized states near the Fermi level [131], with localization length smaller than the distance between the localization centre [132], as shown in figure 10(c). By assuming that the localized states have a spherical shape and are uniformly distributed in the sample, the number of available states within a distance of R is $R^d n(E_F)$, where $n(E_F)$ is the energy density near the Fermi level and d is the dimension of the system. As a result, the energy spacing for hopping between these localized states is given by [133]

$$\Delta E \propto \frac{1}{R^d n(E_F)}. \tag{4.1.2}$$

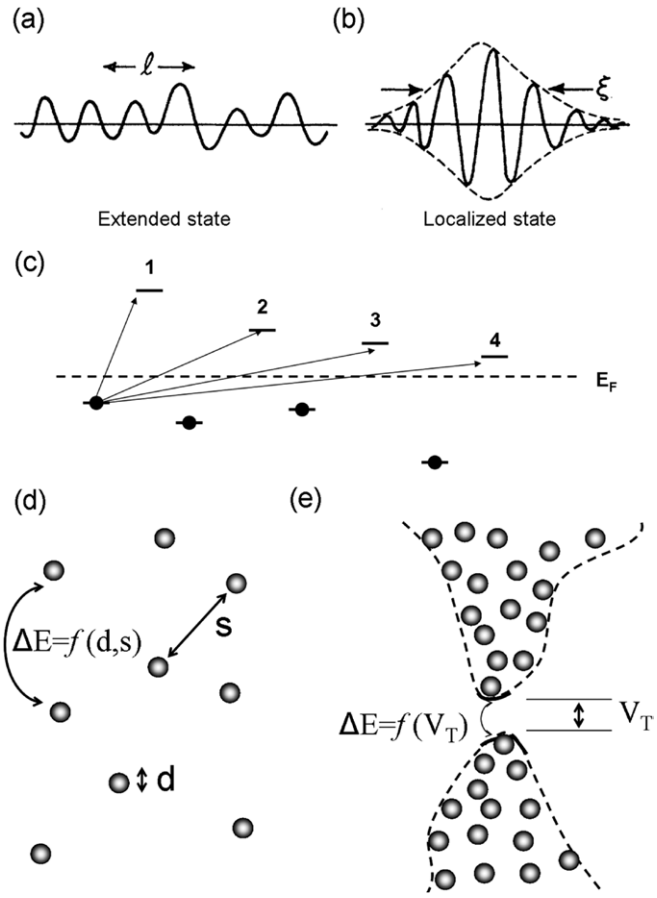

Figure 10. Electrons in the ordered system with extended wave function in (a) and in the disordered system with localized wave function in (b), reprinted with permission from [113], copyright (1985) by the American Physical Society; (c) VRH of electrons in the disordered system, where black dots and short solid lines represent electrons and localized energy states near the Fermi level, respectively. Electron transport in the homogeneous granular system in (d) and in the clustered system in (e).

Here the Coulomb interaction of the excited electron–hole pair is ignored, and the energy spacing for hopping is inversely proportional to R^d. When localized states are close, the energy spacing for hopping is high due to less available energy states, leading to low hopping probability. When the localized states are far from each other, the energy spacing for hopping is low due to an abundance of available localized states. However, as the distance between localized states increases, the overlap between their wave functions will decrease exponentially. By considering the two competing factors, the hopping probability for electrons between the localized states is given by

$$P(R) \propto \exp\left(-\alpha R - \frac{\Delta E}{k_B T}\right) = \exp\left(-\alpha R - \frac{\beta}{k_B T R^d n(E_F)}\right) \tag{4.1.3}$$

where α and β are proportionality constants. When the hopping probability is maximized, the hopping distance is given by

$$R^* = \left(\frac{\beta}{\alpha k_B T n(E_F)}\right)^{1/(1+d)}. \tag{4.1.4}$$

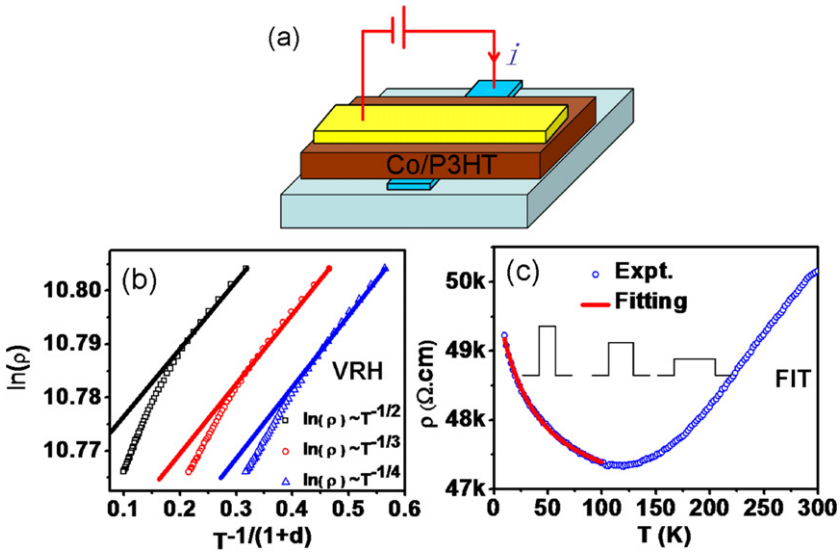

Figure 11. (*a*) Experimental geometry that the resistance of Co/P3HT hybrid film was measured; $\rho \sim T$ fitting of 12 vol% Co/P3HT hybrid into (*b*) VRH model and (*c*) FIT model.

Namely, the hopping distance will decrease as temperature increases due to increased phonon energy. As a result, the mechanism of electron transport in the disordered system is called variable range hopping (VRH). By substituting equation (4.1.4) into (4.1.3) and considering the fact that conductivity is proportional to hopping probability, $\sigma \propto P(R)$, the electrical conductivity of the disordered system is given by

$$\sigma = \sigma_0 \exp\left(-\left[\frac{T_o}{T}\right]^{1/(1+d)}\right). \tag{4.1.5}$$

In Mott's VRH model, the Coulomb interaction between excited electron–hole pair is ignored and the density of states near the Fermi level is assumed to be constant. However, if the Coulomb interaction of the excited electron–hole is strong, there will be a Coulomb gap near the Fermi level and hence the conductivity of a 3D disordered system (Efros–Shklovskii VRH model) is given by [134]

$$\sigma = \sigma_0 \exp\left(-\left[\frac{T_o}{T}\right]^{1/2}\right) \tag{4.1.6}$$

in which $\ln\sigma \sim T^{-1/2}$ replaces the $\ln\sigma \sim T^{-1/4}$ relation for 3D VRH.

Among disordered systems, the case of metallic NPs dispersed in an insulating matrix is a special one, and the electron transport in this granular system is via electron hopping between these metallic NPs as shown in figure 10(*d*). The energy of hopping between metallic NPs is dependent on the particle size and size distribution in the insulating matrix, and is given by [135]

$$E_C = \frac{e^2}{d} F\left(\frac{s}{d}\right) \tag{4.1.7}$$

where e, d and s are the elementary charge, size of particle, distance between particles and F is a function of the shape and distributions of particles, respectively. For this uniformly distributed granular system, its conductivity is given by [135, 136]

$$\sigma = \sigma_0 \exp\left(-\frac{b}{T^{1/2}}\right). \tag{4.1.8}$$

In some granular system, NPs are clustered in some regions, which are separated by insulating gap as shown in figure 10(*e*). Within these clustered regions, it is easy for electrons to hop between NPs due to much reduced distance between NPs; however, the electron transfer between clustered regions is quite limited, and often occurs at the place where the two regions are closest [137, 138]. Further, due to the random motion of electrons in these clustered regions, there will be some transient excess or deficient electronic charges distributed at the surface where the two clustered regions meet, resulting in a fluctuating voltage, V_T, at the junction. The average square of V_T at the junction is given by [137]:

$$\langle V_T^2 \rangle = \frac{k_B T}{C} \tag{4.1.9}$$

where C is the capacitance of the junction and determines the temperature dependence of the energy barrier for electron hopping. In general, the energy barrier will decrease as temperature increases. In this fluctuation-induced tunnelling (FIT) model, conductivity of the granular system is given by [135, 137]

$$\sigma = \sigma_o \exp\left(-\frac{T_1}{T + T_o}\right) \tag{4.1.10}$$

where $k_B T_1$ is the energy required for an electron to tunnel across the polymer gap between conducting particle aggregates and, for $T \ll T_0$, the resistivity is temperature independent.

For electrical measurements, Co/P3HT hybrid film was deposited on a substrate with a pre-made bottom contact by the drop cast method described in section 2.3. After annealing in 5% H_2/95% Ar atmosphere at 150 °C for 2 h, a strip of gold top contact was deposited on the Co/P3HT hybrid film by thermal evaporation in vacuum. Finally, Co/P3HT hybrid films were

connected to a circuit, schematically shown in figure 11(*a*), to measure their resistance over a wide range of temperatures and external magnetic fields in the PPMS system. To investigate the electron transport mechanism in Co/P3HT MNCs, their resistivity was measured as a function of temperature (10–100 K) under no external magnetic field, and was fitted to both VRH and FIT models. According to equation (4.1.5) in the VRH model, the natural logarithm of resistivity is linearly dependent on $T^{-1/(1+d)}$, or $\ln\rho \sim a + bT^{-1/(1+d)}$. Experimental data in the form of $\ln\rho \sim T^{-1/(1+d)}$ relation for 12 vol% Co/P3HT NC were plotted for $d = 1$, 2 and 3 as shown in figure 11(*b*). Although a small segment can be linearly fitted with the $\ln\rho \sim a + bT^{-1/(1+d)}$ relation for all dimensions, the overall fitting of $\ln\rho \sim a+bT^{-1/(1+d)}$ deviated significantly from the experimental data. The resistivity of the 12 vol% Co/P3HT NC, as a function of temperature, is also fitted with the FIT model, namely $\rho = \rho_0 \exp([T_o/T]^{1/(1+d)})$, using a nonlinear curve fitting function of *ORIGIN* software. As shown in figure 11(*c*), the experimental data can be well fitted into the FIT model for temperature between 10 and 100 K. The tunnelling occurs between the clustered cobalt NPs, which is consistent with the microstructures of Co/P3HT MNCs identified in section 2.3.

Above 100 K, the resistivity of Co/P3HT NCs begins to increase with temperature and cannot be fitted into the form $\rho = \rho_0 \exp([T_o/T]^{1/(1+d)})$ any more. This may arise from a pair of competing effects, namely fluctuating barrier height and barrier width. As temperature increases, the height of the energy barriers between cobalt clusters will decrease due to enhanced fluctuating voltage, which decreases the resistivity of Co/P3HT NC. On the other hand, as temperature increases, the separation between cobalt clusters will increase due to the thermal expansion of the P3HT matrix to increase the width of the energy barrier. The height and width of the energy barrier for electron tunnelling between cobalt clusters are shown in the inset of figure 11(*c*). At low temperatures, fluctuating effects dominate, and the resistance decreases with temperature; however, at high temperature, polymer expansion dominates, and the resistance increases with temperature [139].

4.2. MR in Co/P3HT NC film

The resistance of Co/P3HT MNCs with different compositions was measured as a function of external magnetic field up to 8 T at different temperatures from 10 to 300 K. The MR ratio of this hybrid MNC is defined as

$$\mathrm{MR}\% = \frac{\Delta\rho}{\rho} = \frac{\rho(H) - \rho(0)}{\rho(0)} \qquad (4.2.1)$$

where $\rho(H)$ and $\rho(0)$ are the resistivity of the Co/P3HT MNCs at the applied field of H and 0, respectively. Figure 12(*a*) shows the MR ratio of Co/P3HT MNCs with different compositions at 10 K. The resistivity of the composite film decreases as the external magnetic field increases, and continues to decrease slowly even at an external magnetic field of 8 T; at the same time, the magnetization directions of cobalt MNPs are gradually switched from being random to being parallel as the external magnetic field increases. Further, if the concentration of cobalt MNPs increases from 12 vol% Co to 17 vol% Co, the MR ratio of the hybrid film at 8 T increase from 1.8% to 2.9%. Figure 12(*b*), (*c*) and (*d*) show the MR measurement of 15 vol% Co NC film at 20 K, 100 K and 200 K, respectively. Compared with the MR ratio of ∼2.3% measured at 10 K for 15 vol% Co/P3HT MNCs film, the MR ratio at 20 K, 100 K and 200 K decrease to ∼1.5%, 0.5% and 0.13%, respectively. At room temperature, the MR ratio of the hybrid film completely disappears. Further, as temperature increases, the MR ratio becomes more difficult to saturate even at high magnetic fields.

As shown in section 4.1, electron transport in the Co/P3HT MNCs is via the FIT model between the cobalt clusters in the amorphous region of the P3HT matrix. The tunnelling events often occur at the junction where two cobalt clusters are most closely separated. As a result, we propose that the electron tunnelling probability at the joint junction is dependent on the relative magnetization directions of cobalt MNPs. When no external magnetic field is applied to the soft Co/P3HT MNCs, the relative magnetization directions of the surface cobalt MNPs at the joint junction are randomized due to superparamagnetism, as shown figure 12(*e*). In this case, hopping probability of electrons is low and the electrical resistance is high. On the other hand, when a finite external magnetic field is applied to the Co/P3HT MNCs, the magnetization directions of cobalt MNPs are gradually aligned, as shown figure 12(*f*). As a result, the hopping probability of electrons between closest cobalt MNPs will increase, resulting in a lower electrical resistance. Further, it is possible that the electron hopping within cobalt clusters might also contribute to the MR ratio as the magnetization is switched by external magnetic field from being random to being parallel, which is similar to the MR ratio obtained in the self-assembly of cobalt NPs [140].

5. Coupling of magnetic blocking and solvent melting in cobalt FF

A FF, also called magnetic fluid or magnetic colloid, is a stable suspension system containing single domain MNPs in a carrier fluid and showing characteristics of superparamagnetism at room temperature [141–143]. In FFs, MNPs are uniformly dispersed and have both translational and rotational diffusion in the carrier fluid. Consequently, FFs are also called dynamic MNCs. Since their invention in the 1960s [144], FFs have attracted extensive attention in both fundamental research [36, 145] and applications [37]. For practical applications, FFs have been used in several fields such as biomedicine [146], mechanical [147] and sensor [148] technologies, and as room temperature magnetic refrigerants [149]. Although FFs have been investigated for quite some time now, there are still many ambiguities about their fundamental properties including ageing and memory effects [150], related slow dynamics [151], and phase transitions [152–154]. Usually, ZFC and FC measurements are used to detect the magnetic phase transformations in FFs. Typically, as the temperature increases from $T \sim 0$ to 300 K, there is a second order magnetic phase transformation, namely a blocked–unblocked transition for

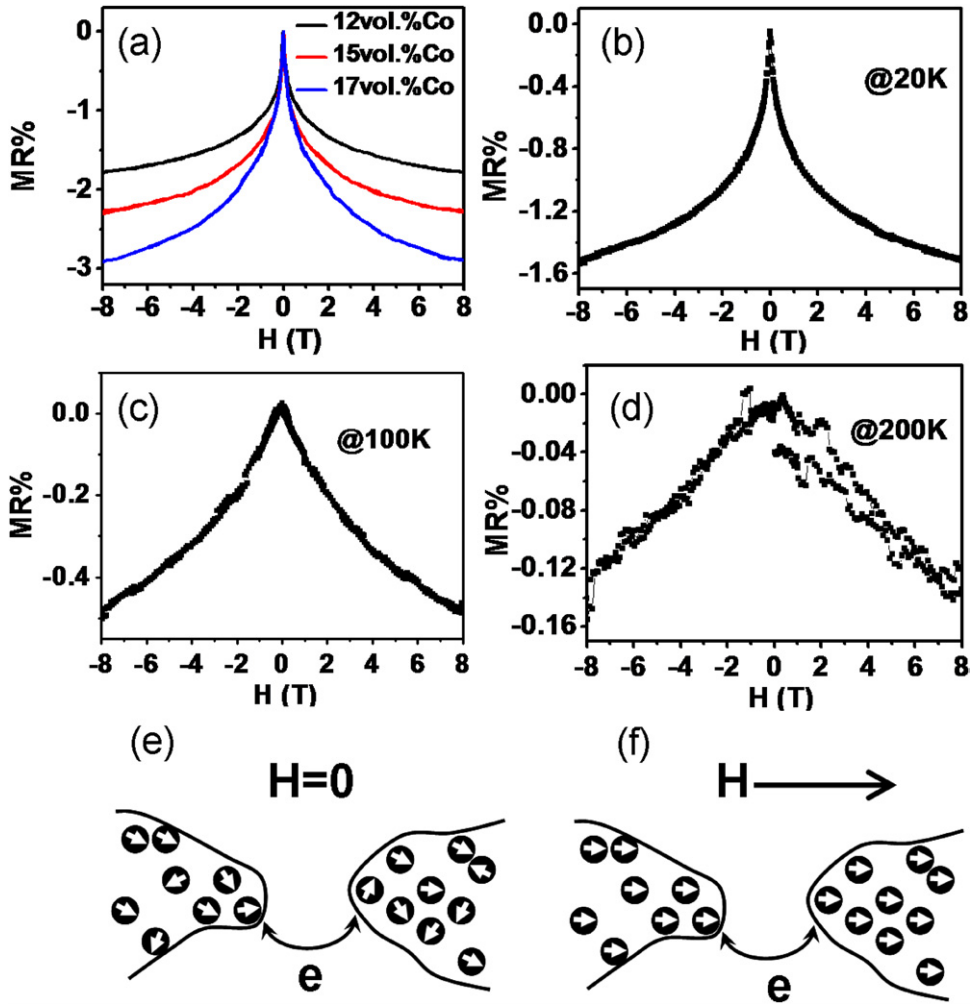

Figure 12. Resistance of Co/P3HT hybrid film with different compositions as a function of external magnetic field at 10 K in (*a*); resistance of 15 vol% Co/P3HT hybrid film as a function of external magnetic field at 20 K in (*b*), 100 K in (*c*) and 200 K in (*d*); (*e*) and (*f*) show the electron hopping between CoMNPs at the closest point between two cobalt clusters for an external magnetic field of 0 and H, respectively.

the superparamagnetic NPs in the fluid, indicated by a broad peak in the ZFC curve [155] with maximum magnetization at the blocking temperature (T_B). The second order magnetic phase transformation at T_B can be tuned by controlling the size, size distribution and interparticle interactions [27] of the superparamagnetic NPs. Additionally, a sharp peak during freezing/melting of the carrier fluid at T_M is also observed in the ZFC curve of the FF [156–158], which is controllable by choosing appropriate organic solvent. In this section, a comprehensive investigation of the magnetic and structural phase transitions in cobalt FFs , for the temperature range of ∼10 K to room temperature, to explore the underlying physics is presented.

5.1. Magnetization relaxation in cobalt FFs

In cobalt FFs, there are two possible relaxation mechanisms for cobalt NPs to reverse their magnetization directions with respect to a fixed coordinate system in space. Firstly, magnetization directions of cobalt NPs can be switched between magnetic easy axes by overcoming the magnetic anisotropic energy barriers with cobalt NPs being physically fixed in space. This mechanism is called Néel relaxation [159, 160], with a relaxation time given by

$$\tau_N = \tau_o \exp\left(\frac{\Delta E}{k_B T}\right) \tag{5.1.1}$$

where the attempt time $\tau_o \sim 10^{-9}$–10^{-11} s, and when an external magnetic field H is applied, $\Delta E = KV(1-h)^2$, where K is the effective magnetic anisotropic constant of NPs, V is the volume of cobalt NPs, $h = H/H_K$ is the reduced field, and H_K is the effective anisotropy field [159]. In the ZFC/FC measurement, the applied external field is usually very small, $H \ll H_K$ and $h \sim 0$; as a result, the Néel relaxation time given in equation (5.1.1) can be simplified as

$$\tau_N = \tau_o \exp\left(\frac{KV}{k_B T}\right). \tag{5.1.2}$$

On the other hand, the magnetization reversal can also be accomplished by physically rotating the cobalt MNPs with the magnetization direction fixed along an easy axis. This mechanism is called Brownian relaxation [159, 161], with the

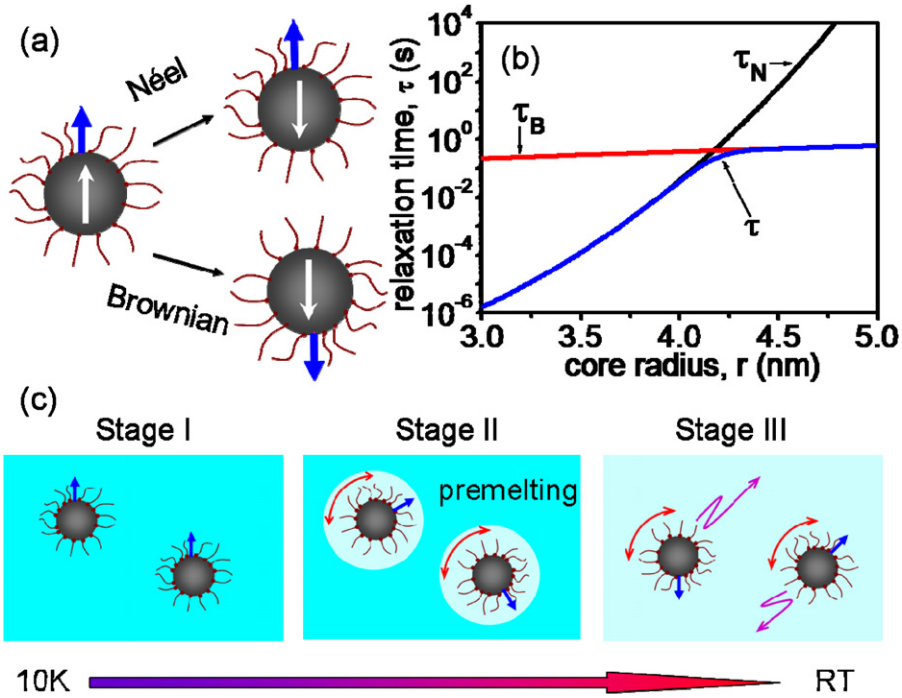

Figure 13. Scheme of Néel and Brownian relaxation of cobalt MNPs in (*a*), the (blue) arrow is a marker indicating the physical position of the particle; (*b*) time scale of Néel (τ_N) and Brownian (τ_B) and overall (τ) relaxation as a function of the core radius of cobalt NPs at room temperature; (*c*) three phases/stages of cobalt FFs as temperature increases from 10 K to room temperature.

relaxation time given by

$$\tau_B = \frac{3\eta V_H}{k_B T} \tag{5.1.3}$$

where V_H is the hydrodynamic volume of cobalt MNPs including the physical size of the cobalt core and the coating of surfactants, η is the dynamic viscosity of the carrier fluid. The two relaxation mechanisms of cobalt MNPs in a fluid are schematically shown and compared in figure 13(*a*).

When both Néel and Brownian relaxation are present, the relaxation mechanism with the shorter relaxation time dominates [143]. Due to the exponential increase of Néel relaxation time and the linear increase of Brownian relaxation time with size of cobalt NPs at the same temperature, Néel relaxation dominates the magnetization reversal for small cobalt NPs, and $\tau = \tau_N$; whilst Brownian relaxation dominates for large cobalt NPs, and $\tau = \tau_B$ [143]. At the crossover of the two relaxation mechanisms, the overall relaxation time τ of cobalt NPs can be calculated by [159]

$$\frac{1}{\tau} = \frac{1}{\tau_N} + \frac{1}{\tau_B}. \tag{5.1.4}$$

For spherical cobalt MNPs in toluene, $\tau_o \sim 10^{-9}$ s, $K \sim 2.7 \times 10^6$ erg cm^{-3} (in [162]), $\eta \sim 0.59 \times 10^3$ Pa s^{-1}, and assuming a functional group of size ~2 nm, the Néel, Brownian and overall relaxation time are plotted as a function of the radius of the cobalt core from 3 to 5 nm at room temperature in figure 13(*b*) with logarithmic scale for relaxation time. As expected, the Néel relaxation time is very sensitive to the size of cobalt NPs, while the Brownian relaxation time, in contrast, is relatively insensitive to the size, leading to a crossover of these two relaxation mechanisms for $r \sim 4$–4.5 nm. For cobalt NPs with size, $r < 4$ nm, Néel relaxation dominates and the overall relaxation spans a large spectrum of frequency; for size $r > 4$ nm, Brownian relaxation gradually becomes dominant due to the difficulty of reversing the magnetization direction over magnetic anisotropic energy barriers (magnetization directions quenched along an easy axis), and the overall relaxation time becomes relatively insensitive to the size of cobalt NPs.

Further, as cobalt FFs are cooled down to ~0 K, the carrier fluid will be completely frozen. In these completely frozen cobalt FFs, cobalt MNPs are randomly distributed in a solid matrix and are spatially fixed with no freedom in both translational and rotational diffusion. Such a completely frozen cobalt FF behaves like a traditional MNC, whose matrix is usually solid at room temperature [163]. In a completely frozen FF, cobalt NPs can only reverse their magnetization directions by Néel relaxation, and no Brownian relaxation is allowed due to spatial confinement. However, as temperature increases, at a critical point below T_M of the carrier fluid, the solid matrix will begin to melt starting from the interface between cobalt NPs and the frozen matrix. This premelting phenomenon at the interface is an intrinsic property for the incoherent interface or a free surface [164]. Further, premelting phenomenon is a continuous process [165], starting at a temperature below T_M [166]. As a result, the first order melting transition observed in the macroscopic scale may be a second order phase transition at the nanoscale.

Based on the discussion above, there are three distinct relaxation phases/stages as temperature increases from 10 K to room temperature, as schematically shown in figure 13(*c*). At temperature below the starting point of premelting, T_{PM}, namely $T < T_{PM}$, of stage I, cobalt FFs are completely frozen

Table 1. Magnetization reversal mechanisms in three stages.

Stage	Temp.	Néel	Brownian	Fixed location
I	$T < T_{PM}$	Yes	No	Yes
II	$T_{PM} < T < T_M$	Yes	Yes	Yes
III	$T > T_M$	Yes	Yes	No

and behave as a traditional MNC. In this stage, cobalt NPs are all physically fixed in space, and only Néel relaxation is possible for magnetization reversal. For stage II, or $T_{PM} < T < T_M$, due to the liquid interface between cobalt NPs and the frozen matrix, cobalt MNPs begin to physically rotate by Brownian relaxation in addition to Néel relaxation, even though the locations of all cobalt NPs are still fixed in space. And finally, for stage III or $T > T_M$, the melting will proceed rapidly to form a complete liquid phase. At this stage, cobalt NPs have the largest degree of freedom to reverse their magnetization directions both by Néel and Brownian relaxation, and the physical locations of all cobalt NPs are constantly evolving. The three stages/phases of cobalt FFs during heating are summarized/tabulated in table 1.

5.2. *Coupling of blocking and melting in cobalt FF*

5.2.1. Experimental measurements. In ZFC measurement, cobalt FFs are cooled down to 10 K under no external magnetic field. An external magnetic field, $H = 100$ Oe, is applied to the sample at 10 K and the magnetization of the cobalt FFs is then measured as a function of increasing temperature. In FC measurement, the magnetization of cobalt FFs is measured as a function of temperature under an external magnetic field, $H = 100$ Oe, either during cooling (FCC curve) or warming (FCW curve). The blocking temperature of cobalt NPs powder is $T_B \sim 250$ K, based on the reading of the maximum value[2] in the ZFC curve in figure 14(*a*), which is consistent with the TEM observation of ∼9 nm cobalt NPs [167] in the inset. The downturn in the FC curve, as temperature decreases, indicates the presence of interparticle interactions [150]. When cobalt NPs are dissolved in an organic solvent with concentration of 20 mg mL^{-1}, the average interparticle separation will increase, leading to a corresponding reduction of interparticle interactions. Consequently, T_B of the dissolved cobalt NPs will shift to a lower temperature, as indicated in the ZFC curve in figure 14(*b*) at $T_B \sim 210$ K [168]. In this experiment, three different organic solvents are chosen such that for a given size and concentration of cobalt NPs their melting points, T_M, are $T_M > T_B$ for o-xylene (figure 14(*b*)), $T_M \sim T_B$ for chloroform (figure 14(*c*)) and $T_M < T_B$ for toluene (figure 14(*d*)). These temperatures are summarized in table 2.

The broad peak at $T_B \sim 210$ K in the ZFC curve of cobalt NPs in o-xylene, as shown in figure 14(*b*), corresponds to the second order blocked–unblocked superparamagnetic transitions. In addition, another sharp peak also appears in the ZFC curve as temperature approaches the bulk melting point of o-xylene at $T_M = 248$ K. For this sharp peak, the dramatic increase in the magnetization in the ZFC curve starts from ∼243 K, which is below T_M of o-xylene and is due to the premelting at the cobalt/o-xylene interface, as shown in figure 13(*c*). After o-xylene is completely melted above $T_M = 248$, the ZFC magnetization of the cobalt FF in o-xylene drops rapidly, which corresponds to the transformation from stage II (premelting) to stage III (completely melting). When cobalt NPs were dissolved in chloroform ($T_M \sim T_B$), the two peaks in the ZFC curves, corresponding to blocking and melting transitions, are superimposed on each other to yield a sharp peak of much greater intensity, followed by a rapid drop after chloroform is completely melted, as shown in figure 14(*c*). Finally, when cobalt NPs are dissolved in toluene ($T_M < T_B$), the two peaks of blocking and melting are separated again; however, the peak of melting is observed at lower temperature with considerably reduced intensity during melting, followed by a rapid drop of magnetization after complete melting of toluene at $T_M = 180$ K. After that, the ZFC magnetization slowly increases until it reaches its blocking temperature at $T_B = 210$ K in the liquid phase. It should be pointed out that the dramatic increase in ZFC magnetization starts below the melting point for all the carrier fluids. By comparing the ZFC curve of cobalt FFs in o-xylene ($T_M > T_B$), chloroform ($T_M \sim T_B$) and toluene ($T_M < T_B$), it can be concluded that the intensity of the sharp peak during melting is strongest when melting and blocking transitions are superimposed. On the other hand, the intensities of the sharp peak during melting are considerably reduced if the melting and blocking transitions are well separated. To verify the latter, FF containing cobalt NPs with smaller sizes in o-xylene was prepared so that the blocking ($T_B \sim 100$ K) and melting ($T_M = 248$ K) are well separated, as shown in figure 14(*f*). As expected, the intensity of the sharp peak during melting is significantly reduced and can only be clearly observed after being magnified as shown in the inset. Schematic ZFC curves, considering the Néel relaxation with the Brownian relaxation superimposed for different fluids with varying T_M, are summarized in figure 14(*e*). Note that the enhancement of the FC magnetization of cobalt FFs, compared with the cobalt NPs in powder form, as shown in figure 14(*b*)–(*d*), is due to the additional possibility of Brownian relaxation of cobalt NPs in the FF under an external magnetic field during cooling.

5.2.2. Coupling effects in Cobalt FFs: M-spectrum theory. M spectrum [150], defined by the integrand in $\overline{M}(t) = \int M_{spec}(t, V)\,dV$ for particles of volume V at time, can be used to interpret the coupling effect observed in cobalt FFs. M-spectrum can be simply calculated by the product of particle volume distribution function, $f(V)$, and the magnetization of a single particle of volume, V, at time t, $M(t, V)$, namely $M_{spec}(t, V) = M(t, V)f(V)$. The magnetization of the sample at any time, t, can be calculated by integrating the M-spectrum with respect to the volume of particles (or the area enclosed by the M-spectrum curve). At each specific temperature of a ZFC measurement, the corresponding M-spectrum can be divided into two segments by a critical volume, V_B, indicated by arrows in figure 15(*a*). For particle

[2] Note: Occasionally, the bifurcation point of ZFC/FC curve is defined as T_B instead of the maximum point in the ZFC curve. However, the bifurcation point is usually poorly defined, and we use the latter to define T_B.

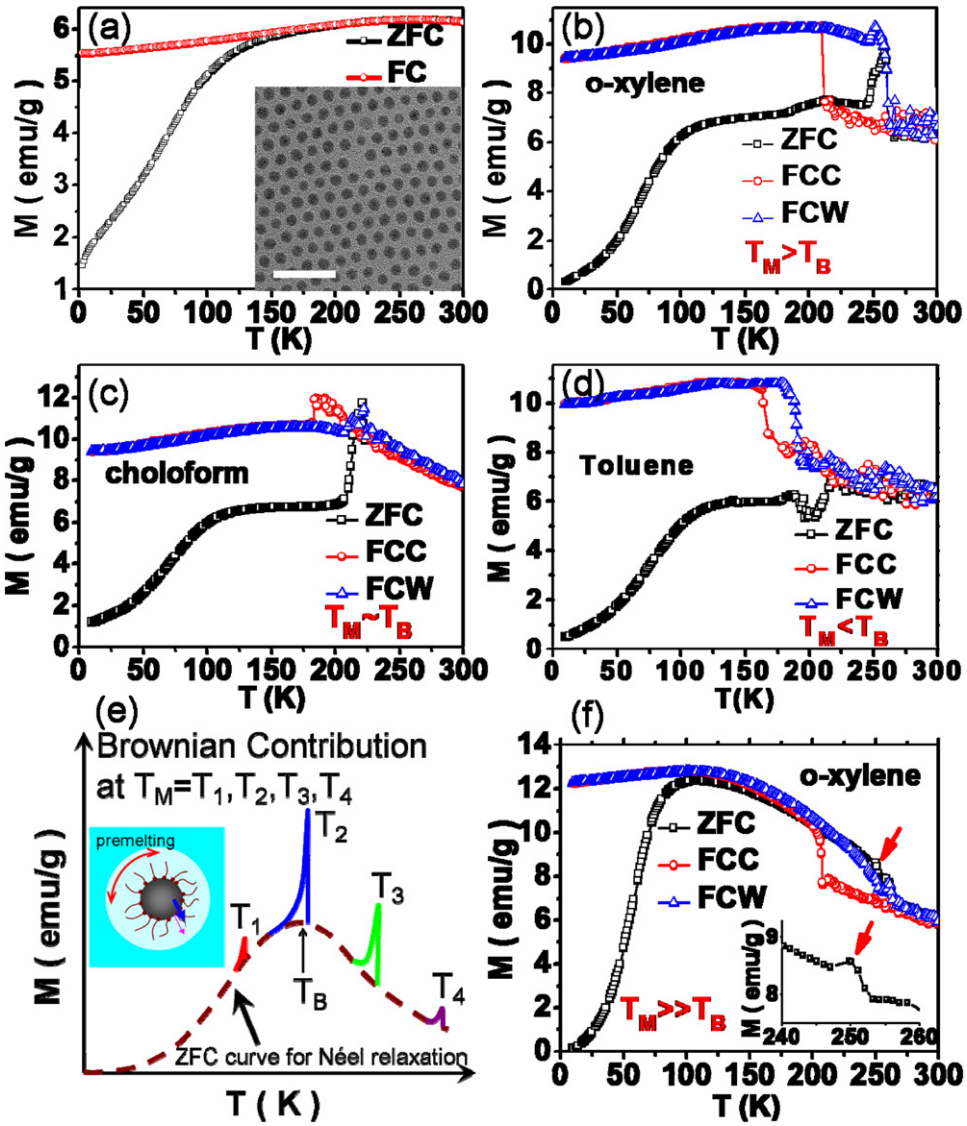

Figure 14. ZFC and FC curves for (*a*) cobalt MNP powders, and in o-xylene (*b*), chloroform (*c*) and toluene (*d*); $H = 100$ Oe for all measurements. FCC and FCW are the FC curves during decreasing and increasing temperatures, respectively. The scale bar of the inset in (*a*) is 50 nm; (*e*) schematic summary of the peak during melting of solvent at different temperatures with respect to the T_B; (*f*) ZFC/FC curves of very small cobalt NPs in o-xylene for well separated T_M and T_B; the inset shows the magnified sharp peak during melting of o-xylene.

Table 2. Melting temperatures of organic solvent.

Organic solvent	o-xylene	Chloroform	Toluene
Melting point (T_M)	248 K	210 K	180 K
Compared with $T_B \sim 210$ K	$T_M > T_B$	$T_M \sim T_B$	$T_M < T_B$

with volume $V < V_B$, the intensity of the ZFC M-spectrum increases as the volume of particles increases, and these particles contribute to the magnetization of the samples. However, for particles with volume $V > V_B$, the intensity of the ZFC M-spectrum will rapidly drop to zero, and these particles do not contribute to the magnetization of the samples due to their randomly blocked state. However, as temperature increases, the critical volume, V_B, defining the cutoff of the ZFC curve, will move to larger values because larger particles will be unblocked at higher temperature, as shown in figure 15(*b*). Further, the intensity of the ZFC M-spectrum will continuously reduce as temperature increases due to enhanced thermal agitation. As a result, the area enclosed by the ZFC M-spectrum will be largest at an optimized temperature to maximize the magnetization of the ZFC curve at T_B. In addition, the ZFC and FC M-spectra are superposed on each other for $V < V_B$; while for $V > V_B$, the intensity of the FC M-spectrum is still nonzero with continuously reduced intensity as temperature increases.

It is worth mentioning that only Néel relaxation of cobalt MNPs has been considered in the calculation of the ZFC M-spectrum in figure 15(*a*) and (*b*). However, at stage II (premelting), in figure 13(*c*), a liquid layer is present at the interface between cobalt NPs and the frozen matrix, giving additional possibility to relax the magnetization directions of cobalt MNPs by physically rotating the whole particle (Brownian relaxation). During Brownian relaxation, the

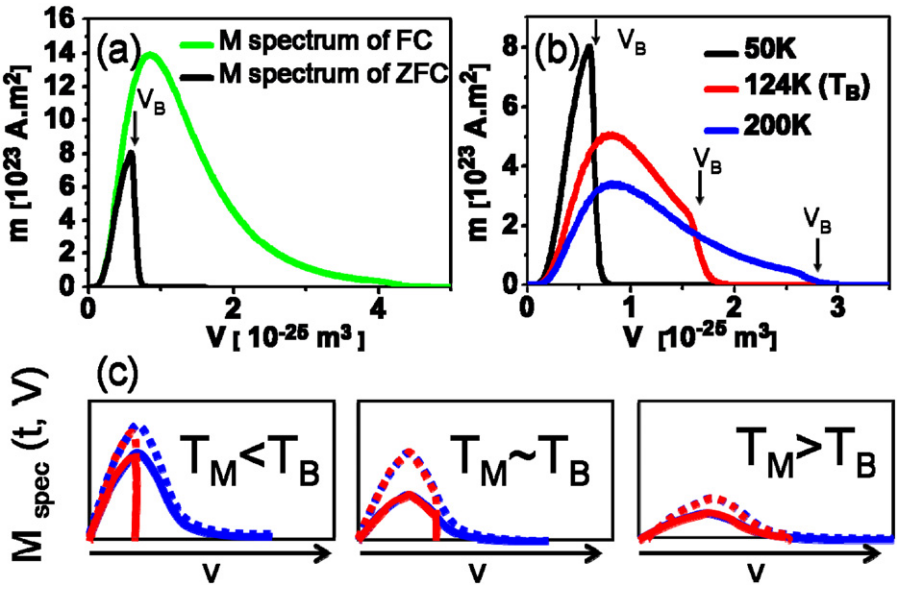

Figure 15. (*a*) The simulated M-spectrum of ZFC and FC magnetization of cobalt NPs in powder form at 50 K in (*a*) and ZFC magnetization of cobalt NPs at 50, 124 and 200 K in (*b*); all simulation is performed by assuming a particle size ∼5 nm with a log normal size distribution and a standard deviation of 1 nm for 10^{18} particles; and (*c*) the schematic M-spectrum of ZFC and FC magnetization of cobalt NPs before (solid line) and after (dashed line) premelting. Due to premelting, the intensity of M-spectrum of both ZFC and FC will be enhanced due to alignment of easy axis of cobalt NPs by Brownian relaxation under an external magnetic field.

magnetization directions of cobalt MNPs will be fixed along its easy axes; but by physical rotation, it allows cobalt MNPs to align their easy axes/magnetization directions along the direction of the external magnetic field. As a result, for the calculation of ZFC and FC M-spectra during stage II (premelting), additional contributions from the alignment of the easy axes along the external field have to be considered, which gives higher intensity in ZFC and FC M-spectra, as shown by the dashed lines in figure 15(*c*). However, small particles do not favour Brownian relaxation due to low-energy barrier for Néel relaxation; thus giving overall a small enhancement of the intensity in ZFC M-spectrum.

The area enclosed by the solid line (without Brownian relaxation) and the dashed line (with Brownian relaxation) in the ZFC M-spectrum is equal to the intensity of the sharp peak during melting observed in figure 14(*b*)–(*d*). For cobalt NPs in toluene, ($T_M < T_B$), V_B is small, namely most cobalt NPs are still blocked during melting of toluene; further, the Brownian relaxation for the unblocked particles with volume $V < V_B$ is trivial. As a result, the area enclosed by the two ZFC M-spectra is small, as shown in figure 15(*c*), giving a sharp peak with reduced intensity, observed in figure 14(*d*). For cobalt NPs in chloroform ($T_M \sim T_B$), V_B moves to higher value, and larger particles are unblocked during melting of chloroform. In addition, the enhancement of M-spectrum intensity of these newly unblocked particles will be much stronger than smaller particles. As a result, the area enclosed by the two ZFC M-spectra is significantly enhanced to give a sharp peak with strongest intensity, observed in figure 14(*c*). Finally, for cobalt NPs in o-xylene ($T_M > T_B$), V_B moves to even higher value, and most particles are unblocked during melting of o-xylene, giving possibilities to obtain a sharp peak of greater intensity. However, at the same time, the intensity of the two ZFC M-spectra will both be reduced due to thermal agitation at higher temperature to offset the enhancement of V_B. As a result, the enclosed area of the two ZFC M-spectra will be reduced to give a sharp peak of reduced intensity, compared with cobalt NPs in chloroform ($T_M \sim T_B$), observed in figure 14(*b*).

5.2.3. Magnetic phase transformation in cobalt FF. During the ZFC measurement of cobalt FFs, two distinctive phase transformations can be observed as the temperature is increased from 10 to 300 K, namely a second order magnetic phase transformation (blocking) and a first order structural phase transformation (melting) indicated by a broad peak and a sharp peak in the ZFC curve, respectively [168]. M-spectrum theory confirms that the strongest sharp peak can be obtained during melting by coupling the blocking and melting transitions [168]. To investigate the first order structural transformation at T_M, $M(H)$ curves of cobalt NPs in o-xylene were measured at various temperatures in the vicinity of T_B as shown in figure 16(*a*). Below and above T_M (=248 K) of o-xylene, $M(H)$ curves change continuously with respect to the measurement at adjacent temperatures. However, by comparing the $M(H)$ curves of cobalt FF before and after melting at $T = T_M$, a jump in saturation magnetization on the $M(H)$ curves can be clearly observed in figure 16(*a*). Since the magnetization is a representation of magnetic order in magnetic materials [169], the sudden change of magnetic order at T_M indicates that a first order magnetic phase transformation occurs at T_M of o-xylene. To explicitly illustrate this first order magnetic phase transformation, magnetization of cobalt FF was measured as a function of temperature under an external magnetic field of 500 Oe as shown in figure 16(*b*). As cobalt FF was warmed up from low temperatures, the change in magnetization is continuous till it reaches $T_M = 248$ K, at

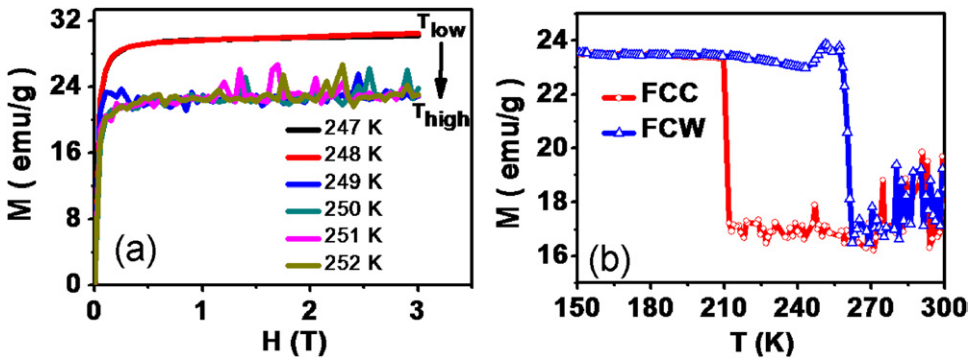

Figure 16. (*a*) $M(H)$ curves of cobalt FF during the melting of o-xylene; and the thermal hysteresis loop of cobalt FF in o-xylene with an external magnetic field of 500 Oe. Reprinted with permission from [168], copyright (2010) by American Institute of Physics.

which a sudden jump of magnetization was observed. Based upon the observation of $M(H)$ curves and $M(T)$ curves, it is proposed that the first order structural phase transition at T_M is also a first order magnetic phase transformation. Further, when it goes across the melting temperature of the carrier fluid, phase II (premelting) will transform to phase III (completely melting) suddenly. As a result, this first order magnetic phase transformation corresponds to the transitions between phase II and phase III. In addition, when it goes across T_B from high temperature, solidification of carrier fluid will not occur until it is well below the bulk melting temperature. This supercooling effect [170] results in the shift of this first order magnetic phase transformation to occur at $T \sim 210$ K as cobalt FF is cooled from high temperature, as shown in figure 16(*b*). The first order magnetic phase transformation and the associated supercooling effect lead to the thermal hysteresis loops in the ZF curves during warming and cooling, as shown in figure 16(*b*). In addition, the continuous (second order) premelting transition is also observed and indicated by the continuous and sharp peak in the ZFC curve.

In summary, three phase transformations can be observed in cobalt FFs as temperature increases from 10 to 300 K, namely a second order magnetic phase transformation (blocked–unblocked transition) at T_B, a first order magnetic and structural phase transformation (phase II-to-phase III transition) at T_M, and a second order premelting transformation at $T_{PM} < T < T_M$. It has been demonstrated that a giant magnetic entropy change can be obtained by coupling a first and a second order magnetic phase transformation to yield a large magnetocaloric effect [171]. As a result, coupling of blocking and melting, by choosing appropriate conditions, in cobalt FFs might be of interest to the magnetocaloric effect for making cheap and efficient magnetic refrigerators [172].

6. Conclusions

Three model systems of cobalt-based magnetic nanocomposites are discussed in this review. First, Au_{core}–Co_{shell} nanoparticles were synthesized by heterogeneous nucleation in organic solvent. As-synthesized Au_{core}–Co_{shell} nanoparticles are not thermally stable due to unreleased energy of the grain boundary in cobalt shell, at the Au/Co interface and in the strained lattice of cobalt and gold. In an *ex situ* heating experiment, the as-synthesized and thermally metastable Au_{core}–Co_{shell} nanoparticles were shown to transform to peanut morphologies in a series of steps to sequentially minimize the energy in grain boundary of cobalt shell, Au/Co interface and strain during heating. Second, Co/P3HT hybrid nanocomposites were fabricated by drop casting the co-solution of cobalt nanoparticles and P3HT and their morphology was investigated by STEM. The cobalt nanoparticles were shown to cluster in the amorphous region of P3HT and are interspersed by the crystalline laminar region of P3HT. Further, the electron transport in the Co/P3HT hybrid film is via fluctuation-induced tunnelling between the clustered cobalt nanoparticles via the crystalline region of P3HT. The resistivity of the Co/P3HT hybrid film decreases when an external magnetic field is applied, and yields a magnetoresistance ratio of ~3% at 10 K. The MR ratio of Co/P3HT nanocomposite decreases with increasing temperature to a trivial value at 200 K and disappears completely at room temperature. Finally, ferrofluids of cobalt nanoparticles dispersed in different solvents were prepared. In the ZFC measurement of these cobalt ferrofluids, a broad peak at T_B and a sharp peak at T_M are observed. The broad peak at T_B corresponds to a second order magnetic phase transformation, namely blocked-to-unblocked transition; while the sharp peak at T_M corresponds to a first order magnetic (structural as well) transformation. The sharp peak associated with the freezing and melting of the solvent is observed to be strongest when the blocking and melting transitions are coupled due to the reactivated Brownian relaxation at the premelting stage. In addition, the sharp enhancement during melting is explained by the reorientation of easy axes to the external magnetic field in the premelted liquid container.

In these studies, the unique properties of the magnetic nanocomposites are often dictated by the interplay between the constituent components. For example, the minimization of the free energy in an Au_{core}–Co_{shell} nanoparticle is all strongly dependent on the atomic arrangements at the Au/Co interface and their morphologies. Another example is the premelting at the interface between carrier fluid and cobalt NPs in the cobalt ferrofluids, which give rise to a sharp peak in the ZFC curve and induces a first order magnetic phase transformation during the premelting of the organic solvent. Such 'interplay effects' will continue to be significant in the behaviour of magnetic nanocomposites and further advances in the field can only

be made by developing an efficient way for their synthesis, probing their fundamental physical behaviour and exploring possible related applications.

Acknowledgments

This project was partially supported by National Science Foundation DMR #0501421 and the Murdock Foundation. Part of this work was conducted at the University of Washington NanoTech User Facility, a member of the NSF National Nanotechnology Infrastructure Network (NNIN). We thank Eric Stach (Brookhaven National Labs), Christine K Luscombe (University of Washington), John W Cahn (University of Washington) and Wenkel Liang (University of Washington) for their expert input in different ways to make some of this research work possible.

References

[1] Komarneni S 1992 *J. Mater. Chem.* **2** 1219
[2] Viswanathan V, Laha T, Balani K, Agarwal A and Seal S 2006 *Mater. Sci. Eng.* R **54** 121
[3] Gangopadhyay R and De A 2000 *Chem. Mater.* **12** 608
[4] Pyun J and Matyjaszewski K 2001 *Chem. Mater.* **13** 3436
[5] Lin Y *et al* 2005 *Nature* **434** 55
[6] Yang P, Zhou X, Cao G and Luscombe C K 2010 *J. Mater. Chem.* **20** 2612
[7] Alexandre M and Dubois P 2000 *Mater. Sci. Eng.* R **28** 1
[8] Giannelis E P 1996 *Adv. Mater.* **8** 29
[9] Ray S S and Okamoto M 2003 *Prog. Poly. Sci.* **28** 1539
[10] Joshi R K, Hu Q, Alvi F, Joshi N and Kumar A 2009 *J. Phys. Chem.* C **113** 16199–202
[11] Lauhon L J, Gudiksen M S, Wang D and Lieber C M 2002 *Nature* **420** 57
[12] Peng X G, Schlamp M C, Kadavanich A V and Alivisatos A P 1997 *J. Am. Chem. Soc.* **119** 7019
[13] Zeng H, Li J, Wang Z L, Liu J P and Sun S 2004 *Nano Lett.* **4** 187
[14] Bao Y, Calderon H and Krishnan K M 2007 *J. Phys. Chem.* C **111** 1941
[15] Yu H, Chen M, Rice P M, Wang S X, White R L and Sun S 2005 *Nano Lett.* **5** 379
[16] Okada A and Usuki A 2006 *Macromol. Mater. Eng.* **291** 1449
[17] Kawasumi M, Hasegawa N, Kato M, Usuki A and Okada A 1997 *Macromolecules* **30** 6333
[18] Sanchez C, Lebeau B, Chaput F and Boilot J P 2003 *Adv. Mater.* **15** 1969
[19] Beecroft L L and Ober C K 1997 *Chem. Mater.* **9** 1302
[20] Zhan G D and Mukherjee A K 2004 *Int. J. Appl. Ceram. Technol.* **1** 161
[21] Zheng W and Wang S C 2003 *Comput. Sci. Technol.* **63** 225
[22] Yeh J M, Chen C L, Chen Y C, Ma C Y, Lee K R, Wei Y and Li S 2002 *Polymer* **43** 2729
[23] Lobez J M and Swager T M 2010 *Angew. Chem. Int. Edn* **49** 95
[24] Krishnan K M 2010 *IEEE Trans. Magn.* **46** 2523–58
[25] Leslie-Pelecky D L and Rieke R D 1996 *Chem. Mater.* **8** 1770
[26] Bedanta S and Kleemann W 2009 *J. Phys. D: Appl. Phys.* **42** 013001
[27] Wen T, Liang W, Li X and Krishnan K M, in preparation
[28] Chen Q and Zhang Z J 1998 *Appl. Phys. Lett.* **73** 3156
[29] García-Otero J, Porto M, Rivas J and Bunde A 2000 *Phys. Rev. Lett.* **84** 167
[30] Mohr R, Kratz K, Weigel T, Lucka-Gabor M, Moneke M and Lendlein A 2006 *Proc. Natl Acad. Sci.* **103** 3540
[31] Hussain F, Hojjati M, Okamoto M and Gorga R E 2006 *J. Comput. Mater.* **40** 1511
[32] Corr S A, Rakovich Y P and Gun'ko Y K 2008 *Nanoscale Res. Lett.* **3** 87
[33] Pyun J 2007 *Poly. Rev.* **47** 231
[34] López D, Cendoya I, Torres F, Tejada J and Mijangos C 2001 *J. Appl. Polym. Sci.* **82** 3215
[35] Ziolo R F, Giannelis E P, Weinstain B A, O'Horo M P, Ganguly B N, Mehrotra V, Russell M W and Huffman D R 1992 *Science* **257** 219
[36] Huke B and Lücke M 2004 *Rep. Prog. Phys.* **67** 1731
[37] Raj K, Moskowitz B and Casciari R 1995 *J. Magn. Magn. Mater.* **149** 174
[38] Zeng H, Sun S, Li J, Wang Z L and Liu J P 2004 *Appl. Phys. Lett.* **85** 792
[39] Milner A, Gerber A, Groisman B, Karpovsky M and Gladkikh A 1996 *Phys. Rev. Lett.* **76** 475
[40] Puntes V F, Krishnan K M and Alivisatos A P 2001 *Science* **291** 2115
[41] Puntes V F, Krishnan K M and Alivisatos A P 2002 *Top. Catal.* **19** 145
[42] Bao Y, Pakhomov A B and Krishnan K M 2005 *J. Appl. Phys.* **97** 10J317
[43] Baker C, Ismat Shah S and Hasanain S K 2004 *J. Magn. Magn. Mater.* **280** 412
[44] Caruso F, Spasova M, Susha A, Giersig M and Caruso R A 2001 *Chem. Mater.* **13** 109
[45] Dey A, De A and De S K 2005 *J. Phys.: Condens. Matter* **17** 5895
[46] Long Y, Chen Z, Duvail J L, Zhang Z and Wan M 2005 *Physica* B **370** 121
[47] Sobal N S, Hilgendorff M, Möhwald H and Giersig M 2002 *Nano Lett.* **2** 621
[48] Puntes V F and Krishnan K M 2001 *IEEE Trans. Magn.* **37** 2210
[49] Bao Y, Beerman M and Krishnan K M 2003 *J. Magn. Magn. Mater.* **266** L245
[50] Park J *et al* 2005 *Angew. Chem. Int. Ed.* **44** 2872–7
[51] Yu W W, Falkner J C, Yavuz C T and Colvin V L 2004 *Chem. Commun.* 2306–7
[52] Narain R, Gonzales M, Stayton P and Krishnan K M 2007 *Langmuir* **23** 6299–304
[53] Khandhar A P, Ferguson M R and Krishnan K M 2011 *J. Appl. Phys.* **109** 07B310
[54] Yin Y, Rioux R M, Erdonmez C K, Hughes S, Somorjai G A and Alivisatos A P 2004 *Science* **304** 711–4
[55] Hu F, Wei L, Zhou Z, Ran Y, Li Z and Gao M 2006 *Adv. Mater.* **18** 2553–6
[56] Ferguson R M, Minard K R and Krishnan K M 2009 *J. Magn. Magn. Mater.* **321** 1548–51
[57] Rodrigues M M A, Simioni A R, Primo F L, Siqueira-Moura M P, Morais P C and Tedesco A C 2009 *J. Magn. Magn. Mater.* **321** 1600–3
[58] Kalale S, Narain R and Krishnan K M 2009 *J. Magn. Magn. Mater.* **321** 1377–80
[59] Gonzales M and Krishnan K M 2005 *J. Magn. Magn. Mater.* **293** 265–70
[60] Gonzales M, Zeisberger M and Krishnan K M 2009 *J. Magn. Magn. Mater.* **321** 1947–50
[61] Falqueiro A M, Primo F L, Morais P C, Mosiniewicz-Szablewska E, Suchocki P and Tedesco A C 2011 *J. Appl. Phys.* **109** 07B306
[62] Massalki T B 1990 *Binary Alloy Phase Diagrams* 2nd edn ed by T B Massalski *et al* (Metals Park, OH: ASM International)
[63] Baibich M N, Broto J M, Fert A, Dau F N V, Petroff F, Eitenne P, Creuzet G, Friederich A and Chazelas J 1988 *Phys. Rev. Lett.* **61** 2472
[64] Valet T and Fert A 1993 *Phys. Rev.* B **48** 7099

[65] Berkowitz A E, Mitchell J R, Carey M J, Young A P, Zhang S, Spada F E, Parker F T, Hutten A and Thomas G 1992 *Phys. Rev. Lett.* **68** 3745
[66] Xiao J Q, Jiang J S and Chien C L 1992 *Phys. Rev. Lett.* **68** 3749
[67] Forrest S R 2004 *Nature* **428** 911
[68] Poddar P, Gass J, Rebar D J, Srinath S, Srikanth H, Morrison S A and Carpenter E E 2006 *J. Magn. Magn. Mater.* **307** 227
[69] Dinega D P and Bawendi M G 1999 *Angew. Chem. Int. Edn* **38** 1788
[70] Sun S and Murray C B 1999 *J. Appl. Phys.* **85** 4325
[71] Puntes V F, Zanchet D, Erdonmez C K and Alivisatos A P 2002 *J. Am. Chem. Soc.* **124** 12874
[72] Bao Y P, An W, Turner C H and Krishnan K M 2010 *Langmuir* **26** 478
[73] Bao Y P 2006 Synthesis, self-assembly, and potential applications of cobalt-based nanoparticles with tailored magnetic properties *PhD Thesis* University of Washington
[74] Shi W, Zeng H, Sahoo Y, Ohulchanskyy T Y, Ding Y, Wang Z L, Swihart M and Prasad P N 2006 *Nano Lett.* **6** 875
[75] Mallik K, Mandal M, Pradhan N and Pal T 2001 *Nano Lett.* **1** 319
[76] Brust M, Walker M, Bethell D, Schiffrin D J and Whyman R 1994 *J. Chem. Soc., Chem. Commun.* 801
[77] Wen T and Krishnan K M 2011 *J. Appl. Phys.* **109** 07B515
[78] Sirringhaus C H *et al* 1999 *Nature* **401** 685
[79] Bao Z, Dodabalapur A and Lovinger A J 1996 *Appl. Phys. Lett.* **69** 4108
[80] Reyes-Reyes M, Kim K and Carroll D L 2005 *Appl. Phys. Lett.* **87** 083506
[81] Braun D, Gustafsson G, McBranch D and Heeger A J 1992 *J. Appl. Phys.* **72** 564
[82] Chen T A, Wu X and Rieke R D 1995 *J. Am. Chem. Soc.* **117** 233
[83] Chen S A and Liao C S 1993 *Macromolecules* **26** 2810
[84] Callister W D Jr 2007 *Materials Science and Engineering: An introduction* 7th edn (New York: Wiley)
[85] Erb T, Zhokhavets U, Gobsch G, Raleva S, Stühn B, Schilinsky P, Waldauf C and Brabec C J 2005 *Adv. Funct. Mater.* **15** 1193
[86] Fell H J, Samuelsen E J, Als-Nielsen J, Grübel G and Mârdalen J 1995 *Solid. State Commun.* **94** 843
[87] Wen T, Liu D, Luscombe C K and Krishnan K M 2009 *Appl. Phys. Lett.* **95** 082509
[88] Yeh S, Wu T, Wei K, Sun Y and Liang K 2005 *J. Polym. Sci.* B **43** 1220
[89] Yoon S, Gonzales-Weimuller M, Lee Y C and Krishnan K M 2009 *J. Appl. Phys.* **105** 07B507
[90] Chantrell R W, Popplewell J and Charles S W 1978 *IEEE Trans. Magn.* **14** 975
[91] Berkowitz A E, Lahut J A, Jacobs I S, Levinson J M and Forester D W 1975 *Phys. Rev. Lett.* **34** 594
[92] Kim H, Achermann M, Balet L P, Hollingsworth J A and Limov V I 2005 *J. Am. Chem. Soc.* **127** 544–6
[93] Gu H, Zheng R, Zhang X and Xu B 2004 *J. Am. Chem. Soc.* **126** 5664–5
[94] Dave S R and Gao X 2009 *Wiley Interdiscip. Rev.: Nanomed. Nanobiotechnol* **1** 583–609
[95] Zeng H, Li J, Liu J P, Wang Z L and Sun S 2002 *Nature* **420** 395–8
[96] McHale J M, Auroux A, Perrotta A J and Navrotsky A 1997 *Science* **277** 788
[97] Ouyang G, Tan X, Wang C X and Yang G W 2006 *Chem. Phys. Lett.* **420** 65
[98] Dahmen U, Xiao S Q, Paciornik S, Johnson E and Johansen A 1997 *Phys. Rev. Lett.* **78** 471
[99] Baletto F and Ferrando R 2005 *Rev. Mod. Phys.* **77** 371
[100] Hill T L 1994 *Thermodynaimics of Small Systems* (New York: Dover)
[101] Hill T L 2001 *Nano Lett.* **1** 273
[102] Hill T L 1962 *J. Chem. Phys.* **36** 3182
[103] Read W T Jr 1953 *Dislocations in Crystals* (New York: McGraw Hill)
[104] Porter D A and Easterling K E 1992 *Phase Transformation in Metals And Alloy* 2nd edn (London: Chapman and Hall)
[105] de Boer F R, Boom R, Mattens W C M, Miedema A R and Niessen A K 1988 *Cohesion in Metals* (Amsterdam: North-Holland) vol 1
[106] Eshelby J D 1957 *Proc. R. Soc. Lond.* A **241** 376
[107] Duan H L, Jiao Y, Yi X, Huang Z P and Wang J 2006 *J. Mech. Phys. Solids* **54** 1401
[108] Yin J S and Wang Z L 1997 *J. Phys. Chem.* B **101** 8979
[109] Banhart F, Hernández E and Terrones M 2003 *Phys. Rev. Lett.* **90** 185502
[110] Wen T and Krishnan K M 2010 *J. Phys. Chem.* C **114** 14838–42
[111] Gertsman V Y and Birringer R 1994 *Scr. Metall. Mater.* **30** 577
[112] Günther B, Kumpmann A and Kunze H D 1992 *Scr. Metall.* **27** 833
[113] Lee P A and Ramakrishnan T V 1985 *Rev. Mod. Phys.* **57** 287
[114] Garnier F, Hajlaoui R, Yassar A and Srivastava P 1994 *Science* **265** 1684
[115] Tang C W 1986 *Appl. Phys. Lett.* **48** 183
[116] Shaheen S E, Brabec C J, Sariciftci N S, Padinger F and Fromherz T 2001 *Appl. Phys. Lett.* **78** 841
[117] Coe S, Woo W K, Bawendi M and Bulović V 2002 *Nature* **420** 800
[118] Choi W B *et al* 1999 *Appl. Phys. Lett.* **75** 3129
[119] Li G, Shrotriya V, Huang J, Yao Y, Moriarty T, Emery K and Yang Y 2005 *Nature Mater.* **4** 864
[120] Rogers J A *et al* 2001 *Proc. Natl Acad. Sci.* **98** 4835
[121] Naber W J M, Faez S and van der Wiel W G 2007 *J. Phys. D: Appl. Phys.* **40** R205
[122] Rocha A R and Sanvito S 2006 *J. Comput. Theor. Nanosci.* **3** 624
[123] Pramanik S, Stefanita C G, Patibandla S, Bandyopadhyay S, Garre K, Harth N and Cahay M 2007 *Nature Nanotechnol.* **2** 216
[124] Rocha A R, García-Suárez V M, Bailey S W, Lambert C J, Ferrer J and Sanvito S 2005 *Nature Mater.* **4** 335
[125] Xiong Z H, Wu D, Vardeny Z V and Shi J 2004 *Nature* **427** 821
[126] Santos T S, Lee J S, Migdal P, Lekshmi I C, Satpati B and Moodera J S 2007 *Phys. Rev. Lett.* **98** 016601
[127] Sakai S, Sugai I, Mitani S, Takanashi K, Matsumoto Y, Naramoto H, Avramov P V and Okayasu S 2007 *Appl. Phys. Lett.* **91** 242104
[128] Tanabe S, Miwa S, Mizuguchi M, Shinjo T, Suzuki Y and Shiraishi M 2007 *Appl. Phys. Lett.* **91** 063123
[129] Kittel C 1953 *Introduction to Solid State Physics* 3rd edn (New York: Wiley)
[130] Anderson P W 1958 *Phys. Rev.* **109** 1492
[131] Mott N F 1967 *Adv. Phys.* **16** 49
[132] Kramer B and MacKinnon A 1993 *Rep. Prog. Phys.* **56** 1469
[133] Mott N F 1969 *Phil. Mag.* **19** 835
[134] Efros A L and Shklovskii B I 1975 *J. Phys. C: Solid State Phys.* **8** L49
[135] Sheng P, Abeles B and Arie Y 1973 *Phys. Rev. Lett.* **31** 44
[136] Abeles B, Sheng P, Coutts M D and Arie Y 1975 *Adv. Phys.* **24** 407
[137] Sheng P 1980 *Phys. Rev.* B **21** 2180
[138] Sheng P, Sichel E K and Gittleman J I 1978 *Phys. Rev. Lett.* **40** 1197

[139] Sichel E K, Gittleman J I and Sheng P 1978 *Phys. Rev.* B **18** 5712
[140] Black C T, Murray C B, Sandstrom R L and Sun S 2000 *Science* **290** 1131
[141] Odenbach S 2004 *J. Phys.: Condens. Matter* **16** R1135
[142] Odenbach S 2009 *Colloidal Magnetic Fluids: Basics, Development and Application Of Ferrofluid* (Berlin: Springer)
[143] Rosensweig R E 1987 *Ann. Rev. Fluid Mech.* **19** 437
[144] Papell S S 1964 Low viscosity magnetic fluid obtained by the colloidal suspension of magnetic particles *US Patent* Specification 3 215 572
[145] Luo W, Nagel S R, Rosenbaum T F and Rosensweig R E 1991 *Phys. Rev. Lett.* **67** 2721
[146] Pankhurst Q A, Connolly J, Jones S K and Dobson J 2003 *J. Phys. D: Appl. Phys.* **35** R167
[147] Hatch A, Kamholz A E, Holman G, Yager P and Böhringer K F 2001 *J. Microelectromech. Syst.* **10** 215
[148] Chung S H, Hoffmann A, Bader S D, Liu C, Kay B, Makowski L and Chen L 2004 *Appl. Phys. Lett.* **85** 2971
[149] Rosensweig R E 2006 *Int. J. Refrig.* **29** 1250
[150] Sasaki M, Jonsson P E, Takayama H and Mamiya H 2005 *Phys. Rev.* B **71** 104405
[151] Robert A, Wandersman E, Dubois E, Dupuis V and Perzynski R 2006 *Europhys. Lett.* **75** 764
[152] Zhang J, Boyd C and Luo W 1996 *Phys. Rev. Lett.* **77** 390–393
[153] Yu Zubarev A and Iskakova L Yu 2002 *Phys. Rev.* E **65** 061406
[154] Klokkenburg M, Erné B H, Meeldijk J D, Wiedenmann A, Petukhov A V, Dulens R P A and Philipse A P 2006 *Phys. Rev. Lett.* **97** 185702
[155] Goya G F, Berquó T S, Fonseca F C and Morales M P 2003 *J. Appl. Phys.* **94** 3520
[156] Morales M B, Phan M H, Pal S, Frey N A and Srikanth H 2009 *J. Appl. Phys.* **105** 07B511
[157] González J M, Montero M I, López-Pérez J A, Mira J, López-Quintela M A and Rivas J 1998 *IEEE Trans. Magn.* **34** 2114
[158] Zhang L, Dou Y, Zhang L and Gu H 2007 *Chin. Phys. Lett.* **24** 483
[159] Kötitz R, Fannin P C and Trahms L 1995 *J. Magn. Magn. Mater.* **149** 42
[160] Fannin P C and charles S W 1989 *J. Phys. D: Appl. Phys.* **22** 187
[161] Brown W F Jr 1963 *Phys. Rev.* **130** 1677
[162] Fiorani D 2005 *Surface Effects in Magnetic Nanoparticles* (Berlin: Springer Science)
[163] Batlle X and Labarta A 2002 *J. Phys. D: Appl. Phys.* **35** R15
[164] Cahn R W 1986 *Nature* **323** 668–9
[165] Dash J G 1999 *Rev. Mod. Phys.* **71** 1737
[166] Frenken J W M and van der Veen F F 1985 *Phys. Rev. Lett.* **54** 134–7
[167] Bao Y and Krishnan K M 2005 *J. Magn. Magn. Mater.* **293** 15
[168] Wen T, Liang W and Krishnan K M 2010 *J. Appl. Phys.* **107** 09B501
[169] Tolédano J C and Tolédano P 1987 *The Landau Theory of Phase Transitions* (Singapore: World Scientific)
[170] Frank F C 1952 *Proc. R. Soc. Lond.* A **215** 43
[171] Pecharsky V K and Gschneidner K A Jr 1997 *Appl. Phys. Lett.* **70** 3299
[172] Pecharsky V K and Gschneidner K A Jr 1999 *J. Magn. Magn. Mater.* **200** 44